minerals

MDPI

Article

Early Cretaceous Thrust and Nappe Structures at Kuantan Shan, Northern Tibetan Plateau

Yiwen Ding, Zhaogang Shao *, Bing Li *, Xuanhua Chen, Daxing Xu and Lele Han

State Key Laboratory of Deep Earth and Mineral Exploration, Chinese Academy of Geological Sciences, Beijing 100037, China; dyw1013429406@foxmail.com (Y.D.)
* Correspondence: shaozhaogang@sina.com (Z.S.); libing@cags.ac.cn (B.L.)

Abstract

Cenozoic reworking has obscured the geometry and timing of Mesozoic contractional structures along the northern margin of the Qilian Shan, limiting reconstruction of Early Cretaceous shortening. We combine field structural observations, growth strata analysis, detrital zircon U-Pb dating by LA-ICP-MS, K–S comparisons, and published seismic interpretations to investigate this deformation in the Kuantan Shan area. Field relationships define a north vergent thrust and nappe system rooted in the North Qilian thrust. Farther north, Paleozoic klippen structurally overlie the Lower Cretaceous Chijinpu Formation along the North Kuantan Shan thrust fault. Footwall drag structures indicate northward transport, while growth strata constrain folding to the early part of the Early Cretaceous. Published seismic profiles show south dipping imbricate and blind thrusts merging into an intracrustal detachment. Detrital zircon age spectra from the Lower Cretaceous footwall sandstones are dominated by Permian grains and show greater statistical similarity to the Bei Shan reference datasets. In contrast, the Paleozoic hanging wall samples contain broader Early Paleozoic and Precambrian age populations that show greater similarity to Paleozoic strata of the Qilian Shan. This provenance contrast, together with the structural relationships, indicates northward emplacement of a thrust sheet derived from the Qilian Shan into the Hexi Corridor. We interpret this contraction as a response to stresses transmitted northward during convergence between the Lhasa and Qiangtang terranes. The Kuantan Shan record extends the known distribution of Early Cretaceous contraction westward. Together with regional evidence of Cenozoic reactivation, it supports structural inheritance during growth of the northern Tibetan Plateau.

Keywords: detrital zircon U–Pb geochronology; structural and growth strata analyses; northern margin of the Qilian Shan; early Cretaceous intracontinental deformation; thrust and nappe system

Check for updates

Academic Editor: Paris Xypolias

Received: 29 September 2026
Revised: 26 October 2026
Accepted: 29 October 2026
Published: 17 November 2026

Copyright: © 2026 by the authors. Licensee MDPI, Basel, Switzerland. This article is an open access article distributed under the terms and conditions of the Creative Commons Attribution (CC BY) license.

1. Introduction

Understanding when and how deformation and high topography developed across the Tibetan Plateau is central to studies of continental collision and intracontinental deformation [1–7]. The Tibetan Plateau lies within the India–Asia collision zone (Figure 1A). Its present high elevation is generally considered to have resulted mainly from Cenozoic collision and subsequent intracontinental shortening [1–4,8,9]. However, increasing geological, thermochronological, sedimentological, and geophysical evidence indicates that the northern Tibetan Plateau was not shaped by a single stage of Cenozoic deformation. Rather, it records multiple phases of tectonic overprinting, including Jurassic and Cretaceous basin

development, Early Cretaceous contraction followed by extension, and later Cenozoic reactivation [9–21]. The Qilian Shan, which defines the northeastern margin of the Tibetan Plateau, preserves important records of both Mesozoic and Cenozoic deformation [9,17,19]. Documenting Early Cretaceous thrust structures along its northern margin is therefore critical for assessing the role of inherited structures in northward plateau growth and for understanding intracontinental strain transfer and deformation in response to distant tectonic forcing.

The Qilian Shan thrust belt defines the northeastern margin of the Tibetan Plateau and forms a major structural and topographic boundary trending NW between the Qaidam Basin to the south and the Hexi Corridor to the north (Figure 1B). Its Cenozoic evolution has been explained by two contrasting models. One proposes progressive northeastward propagation of deformation from the plateau interior, whereas the other emphasizes reactivation of inherited weak zones along a relatively stationary northern plateau boundary [16,22–28]. Distinguishing earlier contraction from subsequent deformation is central to evaluating these models, as studies of superposed thrust and fold structures in the Alpine region have also shown [29–31]. Along the northern Qilian Shan, Early Cretaceous thrusting and growth strata have been documented at Yumu Shan, while folding followed by extension and right slip faulting has been reported at Liyuanpu [18,32,33]. Structural and provenance records from the Pingshanhu Basin indicate changes in deformation and sediment supply during the Early Cretaceous [19]. Farther west, Cretaceous strata in the Yumen Basin contain detritus from the Bei Shan, Qilian Shan, or both regions [34]. Despite these advances, the geometry, kinematics, and timing of thrusting that placed Paleozoic rocks over Lower Cretaceous strata at Kuantan Shan, along the western segment of the northern Qilian Shan margin, remain poorly constrained.

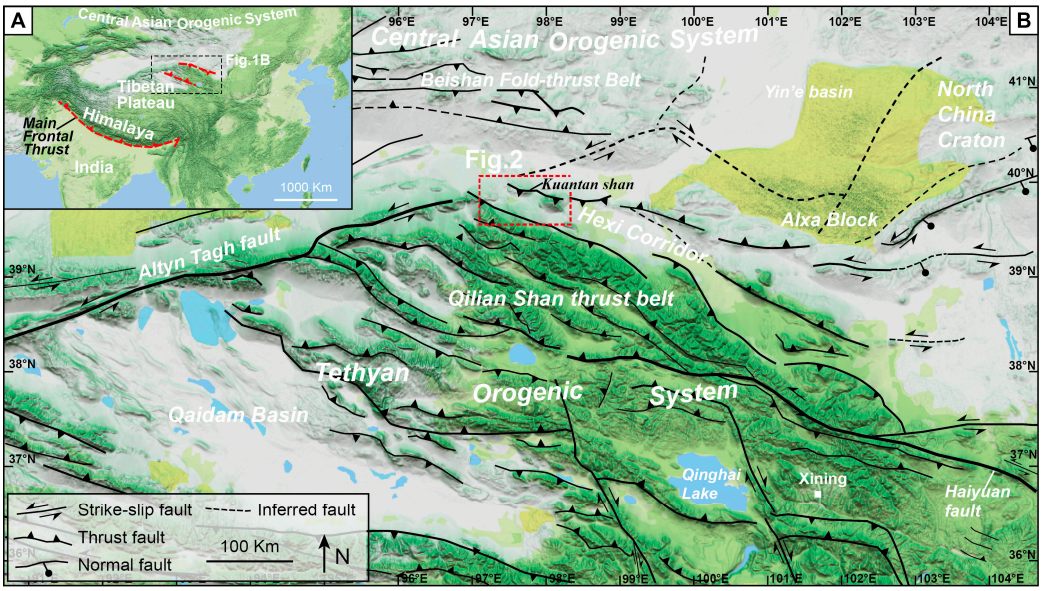


Figure 1. Regional tectonic setting of the northern Tibetan Plateau and adjacent regions. (**A**) Location of the northern Tibetan Plateau within the India–Asia collision zone and surrounding orogenic systems. (**B**) Simplified tectonic map of the northern Tibetan Plateau and the southern Central Asian Orogenic Belt, showing major faults, tectonic domains, basins, and the location of the Kuantan Shan study area. The locations of major faults and tectonic boundaries were compiled from published geological information in [35] and the references therein. Fault traces, tectonic boundaries, and map annotations were independently redrawn by the authors.

To address these questions, we investigated the Kuantan Shan area. This study integrates field structural observations, growth strata analysis, detrital zircon U-Pb geochronol-

ogy, and published stratigraphic and paleocurrent data. Field relationships establish the geometry and kinematics of the thrusts, while growth strata constrain the timing of associated folding. Detrital zircon age spectra are used to compare the provenance signatures of the Paleozoic hanging wall and Lower Cretaceous footwall. Considered with the mapped thrust contacts, these comparisons allow the Qilian Orogen affinity of the Paleozoic hanging wall to be evaluated. The results document Early Cretaceous thrusting at Kuantan Shan and provide new constraints on Mesozoic intracontinental deformation and subsequent structural inheritance along the northern Qilian Shan margin.

2. Geological Setting

The northeastern Tibetan Plateau lies between the Tethyan orogenic system to the south and the southern Central Asian Orogenic Belt to the north. Its geological history includes Paleozoic Ocean closure and accretion, Mesozoic intracontinental deformation, and Cenozoic plateau growth following the India–Asia collision [1,17,19,36]. The Qilian Shan and Hexi Corridor lie along the northern margin of the Tibetan Plateau, with the Bei Shan farther north (Figure 2) [1,34,37]. At Kuantan Shan, Paleozoic structures were subsequently modified during Mesozoic basin development and Cenozoic deformation [12,17,28]. The following sections describe the principal geological features of the Qilian Shan, Hexi Corridor, and Bei Shan.

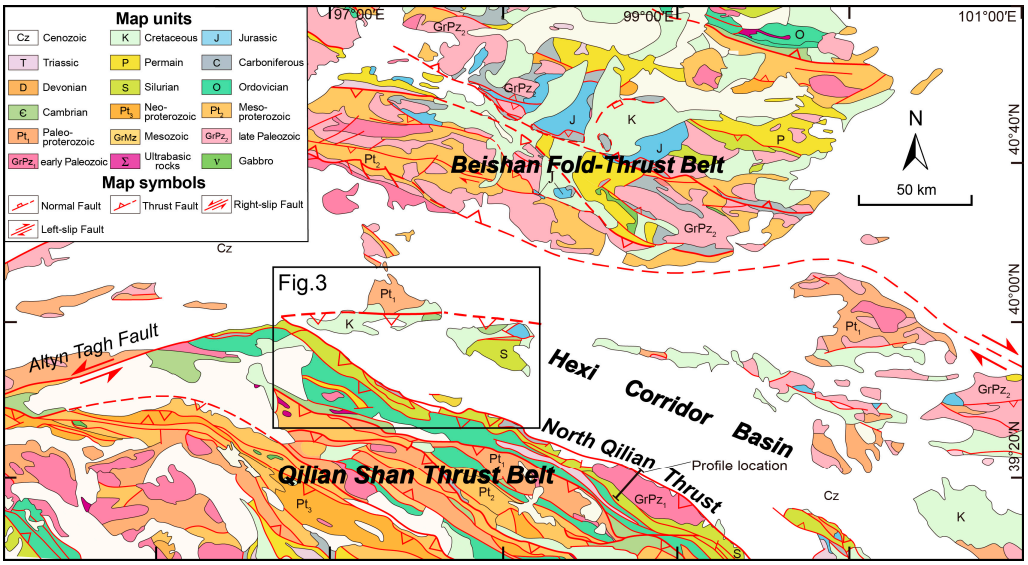


Figure 2. Simplified regional geologic map of the western Hexi Corridor and the adjacent northern Qilian Shan and southern Bei Shan, showing major geologic units, faults, and the location of the Kuantan Shan study area.

2.1. Qilian Shan

The Qilian Orogenic Belt lies along the northeastern margin of the Himalayan and Tibetan orogenic system (Figure 1B) and consists mainly of the northern Qilian Orogenic Belt, central Qilian Terrane, and southern Qilian Orogenic Belt. It represents a typical early Paleozoic accretionary orogenic belt at the northernmost part of the Tethyan tectonic domain and records the subduction, closure, and collision of the Qilian Ocean [1,17,36,38–42]. Its exposed rock assemblages include ophiolitic mélanges, Ordovician–Silurian magmatic arc plutons and volcanic rocks, Silurian flysch, Devonian molasse, and Carboniferous–Permian sedimentary successions.

Jurassic and Cretaceous extension and transtension affected the northern Tibetan Plateau, including the Qilian Shan, and produced continental basins with predominantly

E–W trends and locally preserved extensional structures [10,11,13,14,17,43,44]. Evidence of Early Cretaceous contraction is also preserved along the northern Qilian Shan. At Yumu Shan, a major thrust and nappe system involving folded Lower Cretaceous strata has been interpreted to record contraction before the Cenozoic India–Asia collision [18,32]. Continued convergence between India and Asia reactivated the Qilian Shan thrust belt in the Cenozoic, producing renewed thrusting, folding, and strike-slip faulting. The distribution of this deformation has been linked to inherited suture zones and detachment horizons [12,16,17].

2.2. Hexi Corridor

The Hexi Corridor trends approximately WNW–ESE between the Qilian Shan to the south and the Bei Shan, Longshou Shan, and Alxa Block to the north and northeast (Figure 2; [28]). Cretaceous and Cenozoic sedimentary successions are preserved in a series of basins, including the Jiuquan, Minle, and Wuwei basins from west to east [19,28,45–49].

The Lower Cretaceous Miaogou Group in the Pingshanhu Basin unconformably overlies older strata and comprises alluvial fan, fan delta, fluvial, and lacustrine deposits. Growth strata, folds, and thrust faults record Early Cretaceous contraction, followed by extension represented by normal faults and faults with normal and dextral slip components [19,44]. Sediment provenance also changed through the Early Cretaceous. The earliest deposits were derived mainly from the Alxa Block to the north, whereas the younger Lower Cretaceous succession received an increasing contribution from the Qilian Shan to the south [19]. In the western Yumen Basin, Lower Cretaceous depositional environments, mafic volcanic rocks dated at ca. 116–106 Ma, and growth strata in the hanging walls of normal faults striking NNE–SSW have been interpreted as evidence of Early Cretaceous extension [46,49–51]. Provenance studies indicate that Cretaceous sediments were supplied from the Bei Shan, Qilian Shan, or both regions [34]. Low-temperature thermochronology records Cretaceous cooling and exhumation in the northern Qilian Shan and rapid Early Cretaceous cooling of the Bei Shan basement [22,52–55]. These sedimentary and thermochronological records indicate that basin development in the western Hexi Corridor was accompanied by exhumation of the surrounding source regions.

2.3. Bei Shan

The Bei Shan lies along the southern margin of the Central Asian Orogenic Belt, north of the western Hexi Corridor, and is separated from the northern Qilian Shan by the Yumen Basin and adjacent basins [34,37,56]. Exposed rocks include Precambrian basement, Paleozoic magmatic arc assemblages, ophiolitic mélanges, marine sedimentary successions, and Mesozoic and Cenozoic continental deposits [37,57–59]. The occurrence of Paleozoic metasedimentary rocks in the northern Bei Shan and their reported absence in the south have been interpreted to indicate deeper basement exposure in the southern Bei Shan in the Early Cretaceous [34,56,60].

Jurassic to Early Cretaceous intracontinental contraction reactivated the older Bei Shan orogen and formed the Bei Shan fold and thrust belt [61–64]. Subsequent Early Cretaceous extension produced graben and half-graben basins, in which Lower Cretaceous strata locally rest unconformably on older thrust sheets [64–68]. This transition from contraction to extension resembles the late Mesozoic deformation history of the northern Qilian Shan and Hexi Corridor [12,18,19,64]. The Bei Shan supplied sediment to the Yumen Basin throughout parts of the late Mesozoic and Cenozoic [34,46,48]. Lower Cretaceous strata in the northern basin were derived mainly from the Bei Shan, whereas those in the westernmost basin record contributions from both the Bei Shan and northern Qilian Shan [34,46,48]. These provenance records indicate that the Bei Shan formed an upland source region north of the western Hexi Corridor in the Early Cretaceous. Along the northern margin of the

Jiuxi Basin, the Kuantan Shan and Hei Shan area marks an inherited basin boundary that was reactivated during Cenozoic intracontinental deformation [12,28,49,69].

3. Field Mapping and Structural Geology

Structural analysis provides a methodological framework for examining and interpreting the spatial relationships and evolution of geological structures in terms of their geometry, kinematics, and dynamics. In this study, structural mapping and analysis focused on the Kuantan Shan, which lies along the western segment of the northern Qilian Shan margin adjacent to the Hexi Corridor. Exposed rocks include Paleozoic successions, Mesozoic and Cenozoic strata, and granitoids (Figure 3). Structural mapping at Kuantan Shan combined field observations at the outcrop scale with revision of geological contacts and boundaries between mapped units shown on the 1:250,000 Huahai Sheet geological map [70]. Structural interpretations were based primarily on observed lithologic contacts, structural attitudes, and crosscutting relationships [71]. The attitudes of bedding, foliation, and fault planes were measured with a geological compass and are reported as dip direction/dip angle. Structural measurements were grouped by outcrop. The following sections describe the local stratigraphy, the geometry and kinematics of the principal structures, and the growth strata that constrain the timing of thrusting.

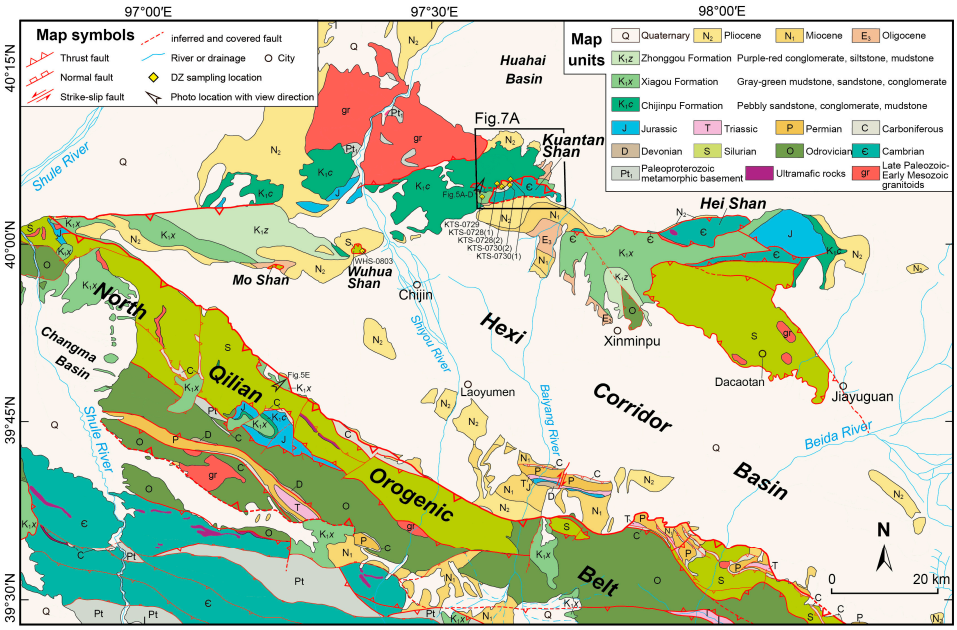


Figure 3. Simplified geologic map of the Kuantan Shan klippe and adjacent areas, showing major faults and sample locations. Principal lithologies of the three Lower Cretaceous formations are listed in the legend.

3.1. Stratigraphy

Lower Cretaceous continental strata are widely exposed in the Kuantan Shan and Hei Shan areas and record basin development, sediment dispersal, and Mesozoic deformation [18,19,72]. Cretaceous sandstones and mudstones are locally deformed by thrusting. The composite Lower Cretaceous succession exceeds 1.9 km in thickness and comprises, in ascending order, the Chijinpu Formation, Xiagou Formation, and Zhonggou Formations (Figure 4). The Chijinpu Formation (>638 m) consists of a lower interval dominated by yellowish brown pebbly sandstone, coarse sandstone, variegated conglomerate, and siltstone, and an upper interval composed mainly of grayish green to dark gray mudstone, shale, conglomerate, and siltstone. The overlying Xiagou Formation (>696 m) comprises

grayish green mudstone, sandstone, and conglomerate with minor siltstone. The Zhonggou Formation (>590 m) consists of purplish red conglomerate, siltstone, and mudstone.

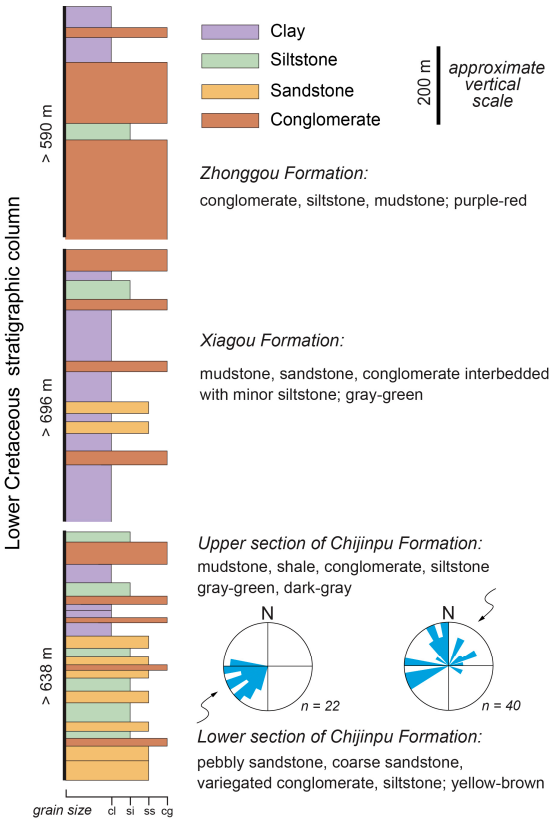


Figure 4. Lower Cretaceous stratigraphic column of the Kuantan Shan area, showing the major lithologic units and paleocurrent patterns.

Regional sedimentological data indicate that the Lower Cretaceous succession accumulated in continental alluvial fan, fluvial, and lacustrine environments [46]. Paleocurrent data for the Chijinpu Formation were compiled from Peng [46]. The lower part of Chijinpu Formation records predominantly southward and southwestward paleocurrents ($n = 22$), whereas the upper part shows more variable directions, including northward paleocurrents ($n = 40$; Figure 4). The change in paleocurrent directions suggests a shift from predominantly northern sources to sources along both basin margins, possibly reflecting tectonic control on sediment dispersal during deposition of the Chijinpu Formation.

3.2. Structural Geology

Field observations and structural analysis in the Qilian Shan, Wuhua Shan, and Kuantan Shan indicate two principal shortening directions, NNE–SSW. Cenozoic faulting has substantially modified the regional structures [12,18,73]. At Kuantan Shan, gently dipping thrusts place Paleozoic rocks above the Lower Cretaceous Chijinpu Formation. These thrusts locally form the basal contacts beneath klippen and are accompanied by folds.

A gently dipping thrust along the northern margin of Kuantan Shan is referred to here as the North Kuantan Shan thrust fault (NKTF). At a representative exposure, the fault dips 148°/20° and strikes NE–SW. The hanging wall consists mainly of dark gray schist with penetrative schistosity. These rocks are assigned to the Cambrian based on their lithology and correlation with Cambrian units on regional geological maps [74]. The NKTF places the Cambrian schist above light grayish green sandy mudstone and argillaceous sandstone of the Lower Cretaceous Chijinpu Formation. West of the main Kuantan Shan

massif, isolated remnants of the hanging wall thrust sheet occur discontinuously over approximately 2 km (Figure 5A–D). At the exposure shown in Figure 5B, footwall beds adjacent to the fault dip 64° toward 135°. Their position above the Lower Cretaceous strata across a basal thrust, together with their isolated distribution, identifies the Cambrian bodies as klippen preserved after erosion of the thrust sheet [75].

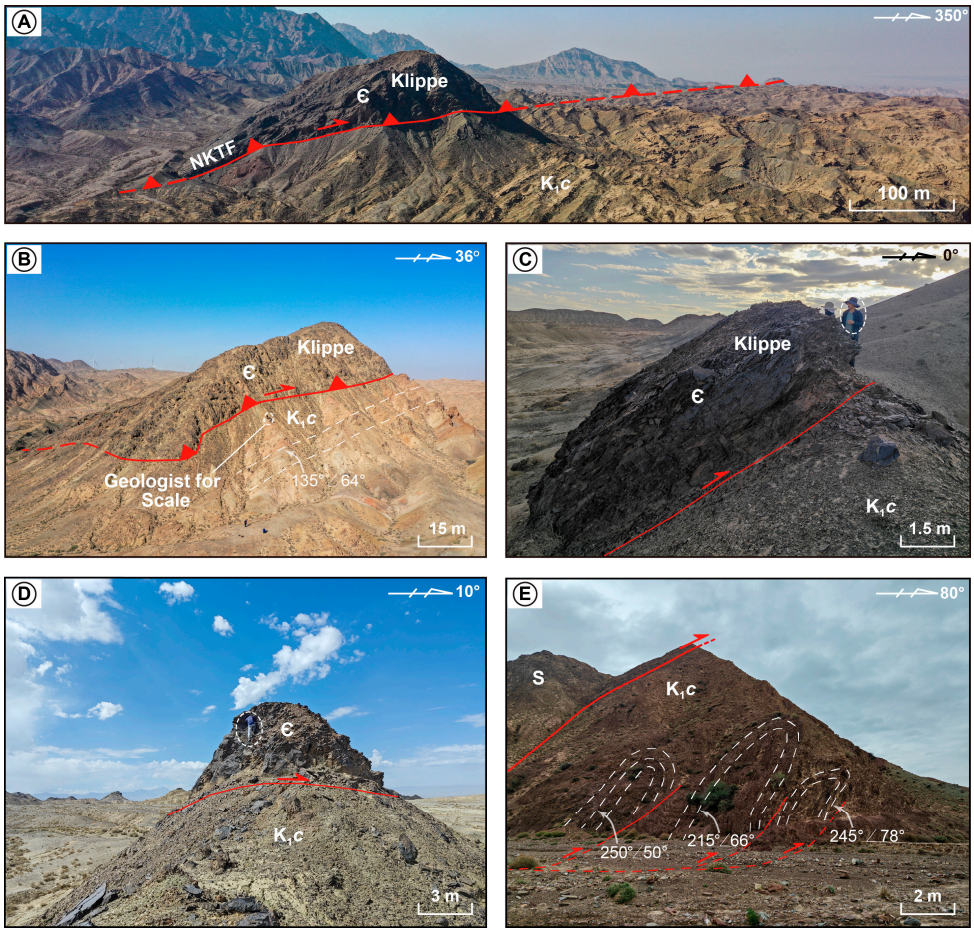


Figure 5. Field photographs of the Kuantan Shan thrust and nappe system. (**A**–**D**) The gently south-dipping North Kuantan Shan thrust fault (NKTF), which dips gently southward, places Cambrian schist over light grayish green sandy mudstone and argillaceous sandstone of the Lower Cretaceous Chijinpu Formation. Isolated remnants of the hanging wall thrust sheet form klippen west of the main Kuantan Shan massif. (**E**) In the root zone, the North Qilian thrust (NQT) places Middle Silurian strata over the Chijinpu Formation, with tight folds developed in the Lower Cretaceous footwall. Red solid and dashed lines mark the observed and inferred traces of thrust faults, respectively. Red arrows indicate the inferred hanging-wall transport direction, and white dashed lines mark bedding traces.

The North Qilian thrust (NQT) is a regional thrust with northeastward vergence that separates the North Qilian orogenic belt from the Mesozoic and Cenozoic basin succession of the Hexi Corridor [12]. Along the southern margin of the western Jiuxi Basin, the Hanxia–Dahuanggou fault forms the westernmost segment of the NQT [73]. This segment is interpreted as the root zone of the Kuantan Shan thrust and nappe system. At the exposure shown in Figure 5E, the thrust places Middle Silurian strata above the Lower Cretaceous Chijinpu Formation. The footwall strata form a series of tight folds. Bedding attitudes measured on one limb of each of three separate folds are 250°/50°, 215°/66°, and 245°/78°, respectively.

In the footwall of the NKTF, bedding in the Lower Cretaceous Chijinpu Formation attitude changes toward the NKTF. Away from the thrust, the strata dip steeply south-

southwestward with an attitude of 202°/67° (dip direction/dip angle). Toward the thrust, the bedding attitude changes to 170°/57° and then to 177°/9° immediately beneath the fault. This progressive decrease in bedding dip toward the thrust defines a footwall drag structure. The footwall drag geometry provides kinematic evidence for northward transport of the hanging wall along the south-dipping NKTF (Figure 6A,B).

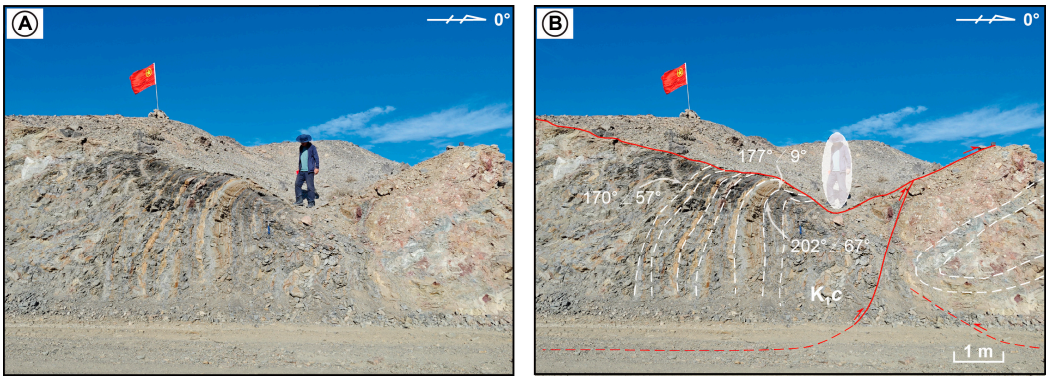


Figure 6. Original (**A**) and interpreted (**B**) field photographs showing footwall drag deformation of the Lower Cretaceous Chijinpu Formation within the Kuantan Shan thrust and nappe system. In (B), red solid and dashed lines mark the observed and inferred traces of thrust faults, respectively. Red arrows indicate the inferred transport direction of the hanging wall. White dashed lines trace bedding, and the white arrow and azimuth in the upper-right corner indicate the viewing direction.

3.3. Growth Strata

Growth strata accumulate during fault movement and fold growth and provide a sedimentary record of active deformation. In contractional settings, progressive rotation of fold limbs during deposition can produce an upward decrease in bedding dip and a fanning arrangement of beds. Systematic variations in bed thickness also record fold growth during sedimentation [76–79]. Where depositional ages are independently constrained, these relationships help determine the timing and duration of deformation [80,81]. At Kuantan Shan, the bedding geometry of the Lower Cretaceous Chijinpu Formation provides evidence for deposition during folding associated with thrusting.

Section A–A′ trends N20°E and crosses a thrust that dips south and places Middle Cambrian strata above the Lower Cretaceous Chijinpu Formation (Figure 7A,B). Footwall beds adjacent to the thrust dip 80–85° southward, consistent with the steep bedding exposed near the fault (Figure 7D). Farther northeast, the beds dip northward, and their dips progressively decrease from 78° to approximately 20° (Figure 7C). Bedding surfaces converge toward the thrust and diverge northeastward, forming a stratal wedge with a fanning geometry. Seven bedding attitudes measured at different locations within the growth strata were plotted as circles and poles on an equal area Schmidt net for the lower hemisphere (Figure 7B). Each pole is normal to the corresponding bedding plane and represents its orientation. Two poles plot in the northern sector of the net and represent beds dipping southward, whereas five plot in the southern sector and represent beds dipping northward. The contoured distribution of poles shows the relative concentrations of these two sets of bedding orientations. The pole to the great circle of best fit defines a subhorizontal π axis trending approximately E–W. The progressive decrease in bedding dip and the fanning geometry are interpreted to record rotation of the fold limb during sedimentation. This part of the Chijinpu Formation is therefore interpreted as growth strata deposited during Early Cretaceous folding and thrusting. Comparable Lower Cretaceous growth strata occur in the Xinminpu Formation at Liyuanpu and Yumu Shan and in the Miaogou Group of the Pingshanhu Basin [18,19,33]. Together with the Early Cretaceous Yumu Shan thrust

and nappe system documented in previous studies [32,33], these occurrences indicate that contraction accompanied basin sedimentation at several localities along the boundary between the northern Qilian Shan and the Hexi Corridor. Parts of the earlier structures were subsequently reactivated during Cenozoic shortening [9,35].

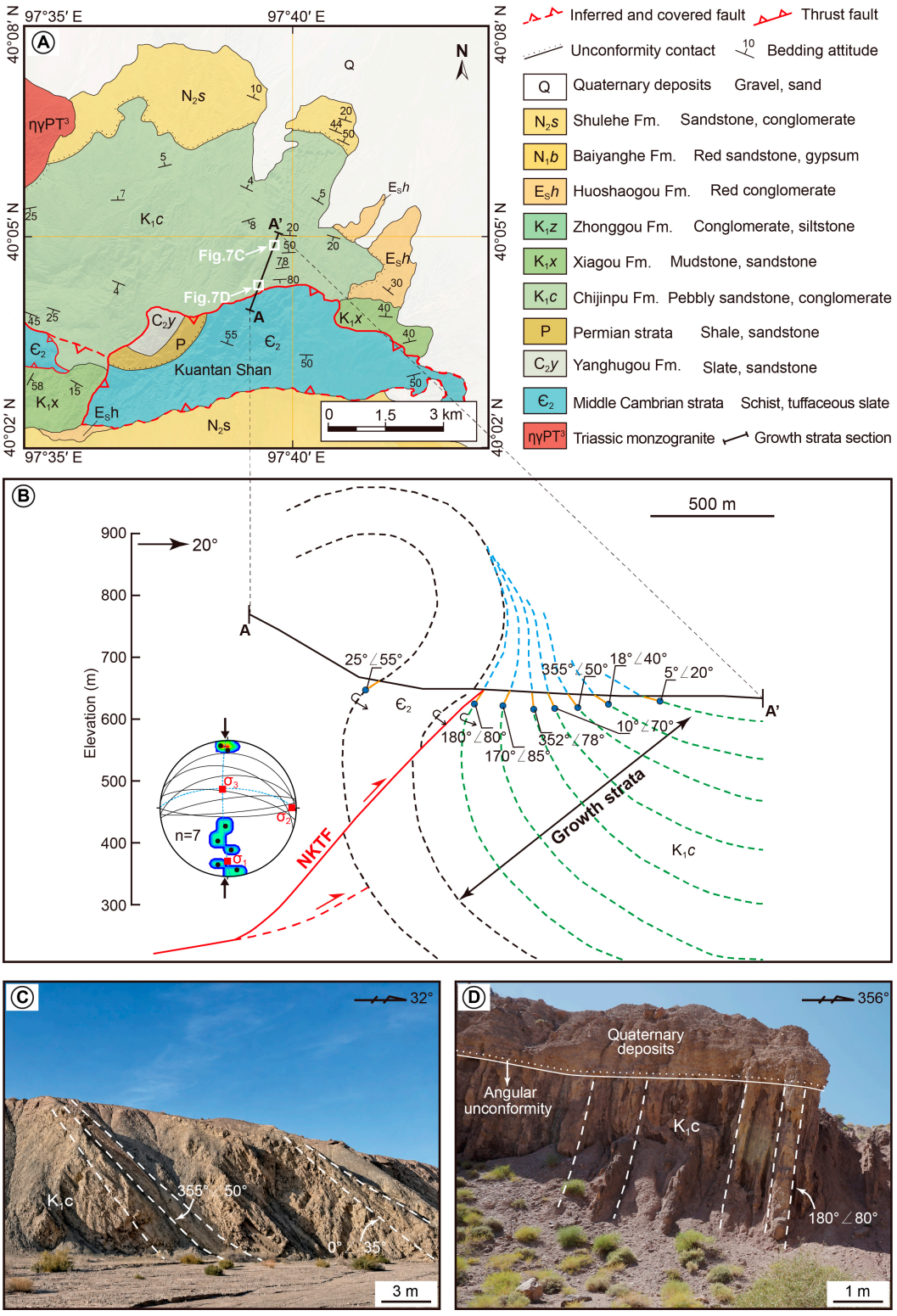


Figure 7. Growth strata in the Lower Cretaceous Chijinpu Formation at Kuantan Shan. (**A**) Geological map showing the distribution of the principal geologic units, the trace of the A–A′ growth strata cross

section and the locations of field photographs. The Lower Cretaceous Chijinpu, Xiagou, and Zhonggou formations consist mainly of conglomerate, sandstone, siltstone, and mudstone. Principal lithologies of the other mapped units are given in the legend. (**B**) Interpreted geologic cross section along A–A′, showing a south-dipping thrust that places Middle Cambrian schist and tuffaceous slate over the Lower Cretaceous Chijinpu Formation. The inset is a lower-hemisphere, equal-area stereographic projection of seven bedding attitudes. The calculated fold axis trends 087° and plunges 8°. Opposing arrows indicate the inferred N–S shortening direction. (**C**) Field photograph showing a decrease in bedding dip from 60° to 35° within the Chijinpu Formation. (**D**) Steeply south-dipping beds in the thrust-proximal part of the succession. Bedding attitudes are expressed as dip direction followed by dip angle. The geologic base map in (**A**) was compiled from the 1:250,000 Huahai Sheet and revised using our field observations. In (**B**), red solid and dashed lines represent the exposed and inferred traces of the thrust, respectively. Black, blue, and green dashed curves trace selected bedding surfaces in different parts of the section. Opposing black arrows indicate the inferred shortening direction. In the stereographic projection, red points represent poles to bedding, blue contours show pole density, and the black great circle represents the best fit to the bedding poles. In (**C**,**D**), white dashed lines trace bedding. Arrows accompanied by azimuths indicate the viewing directions.

4. Deep Seismic Reflection Profile Interpretation

Deep seismic reflection profiles across the northern Qilian Shan and the Hexi Corridor margin have commonly been used to discuss Cenozoic shortening and outward growth of the northeastern Tibetan Plateau. In addition to this Cenozoic signal, these profiles also show how Paleozoic and older rocks are juxtaposed against Jurassic–Cretaceous and Cenozoic sedimentary rocks along thrust faults. Here, a previously published seismic reflection profile [82] is used to compare seismic scale fault geometries with the thrust contacts documented at Kuantan Shan. The approximate depth scales are converted from two-way travel time using an average P-wave velocity of 5.5 km/s. Therefore, the following interpretation emphasizes reflector continuity, truncation, and fault bounded stratigraphic juxtapositions rather than exact depths.

The seismic reflection profile shown in Figure 8 crosses the frontal thrust system of the northern Qilian Shan. Jurassic–Cretaceous strata form laterally continuous, finely laminated reflectors in the foreland. Toward the hanging wall, these reflectors are folded, truncated, and locally repeated. Farther south, another thrust cuts the hanging wall of the frontal structure and places Ordovician and Silurian rocks above Cretaceous strata. This geometry is consistent with surface observations in the Kuantan Shan, where Silurian and other Paleozoic strata are thrust over Lower Cretaceous Chijinpu Formation.

The Profile provides seismic scale corroboration for superposed Mesozoic thrusting and Cenozoic reactivation along the northern Qilian Shan and the Hexi Corridor margin. The profile images imbricate thrusting in the upper crust along the boundary between the northern Qilian Shan and the Hexi Corridor. Combined with the Lower Cretaceous growth strata and the thrust contacts placing Paleozoic rocks above the Chijinpu Formation at Kuantan Shan, these structures are interpreted to record Early Cretaceous contraction followed by Cenozoic reactivation. Renewed thrusting along the range front and deformation of the Cenozoic succession indicate that subsequent shortening further modified the earlier thrust system.

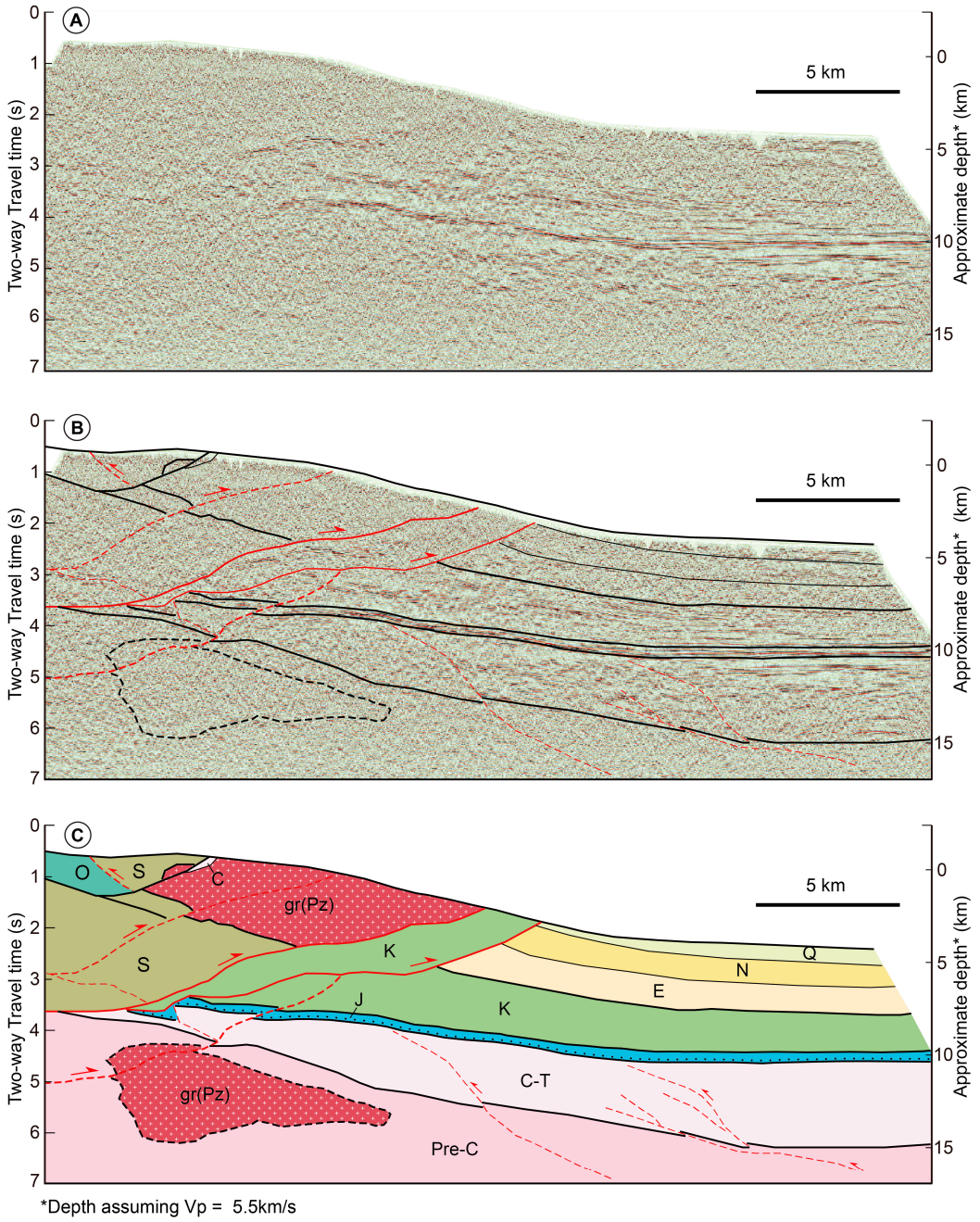


Figure 8. Seismic reflection profile across the northern Qilian Shan front showing Silurian and other Paleozoic rocks thrust over Cretaceous strata. (**A**) Uninterpreted seismic reflection profile. (**B**) Interpreted seismic reflection profile showing the main reflectors and south-dipping thrust faults. (**C**) Geologic cross section based on the interpretations shown in (**B**), showing Silurian and other Paleozoic rocks structurally emplaced above Cretaceous strata. Approximate depth is converted from two-way travel time assuming an average P-wave velocity of 5.5 km/s. Colors in (**C**) denote the labeled geologic units. In (**B**), solid and dashed black lines trace interpreted and inferred seismic reflectors, respectively. In (**C**), they mark interpreted and inferred geologic contacts. Solid and dashed red lines denote interpreted and inferred thrust faults, respectively, and red arrows indicate the direction of hanging-wall transport. The profile location is shown in Figure 2. Modified after [82] with permission from the Geological Society of America.

5. Sampling Strategy and Analytical Methods

Six samples, including five sedimentary rock samples and one metasedimentary rock sample, were collected from the Kuantan Shan and adjacent areas. Detailed sample locations,

stratigraphic assignments, and lithologies are listed in Table 1, and the sample locations are shown in Figure 3. These samples comprise three Cretaceous sandstones, one Permian shale, one Carboniferous slate, and one Silurian sandstone.

Table 1. Summary of U-Pb zircon geochronology samples in this study.

Sample	Latitude (°N)	Longitude (°E)	Elevation (m)	Stratigraphy	Lithology
KTS-0728(1)	40°03′49.90″	97°36′44.09″	1902	Cretaceous	Sandstone
KTS-0729	40°03′23.41″	97°35′28.34″	1896	Cretaceous	Sandstone
KTS-0730(1)	40°04′16.11″	97°39′09.85″	1812	Cretaceous	Sandstone
KTS-0728(2)	40°03′44.51″	97°37′31.26″	1905	Permian	Shale
KTS-0730(2)	40°03′50.13″	97°38′55.92″	1914	Carboniferous	Slate
WHS-0803	39°58′40.68″	97°23′17.37″	1732	Silurian	Sandstone

5.1. Detrital Zircon U-Pb Analytical Method

Six rock samples were collected for zircon separation, including four sandstones, one shale, and one slate. Each sample weighed approximately 4–6 kg. Zircon separation was undertaken at the Hebei Institute of Regional Geological Survey, China, using standard density and magnetic separation techniques. Representative zircon grains were handpicked under a binocular microscope and mounted in epoxy resin discs. The mounts were polished to expose the interiors of the grains. Cathodoluminescence images were obtained to examine internal textures and select appropriate analytical sites.

Zircon U-Pb dating was performed by LA-ICP-MS at the Mineral and Fluid Inclusion Microanalysis Laboratory, Institute of Geology, Chinese Academy of Geological Sciences, Beijing, China. The analyses employed an NWR 193UC laser ablation system (Elemental Scientific Lasers, Bozeman, MT, USA) operating at 193 nm and coupled to an Agilent 7900 ICP-MS (Agilent Technologies, Santa Clara, CA, USA). Before analysis, the zircon mounts were cleaned, and each analytical site was preablated to remove possible surface contamination. A spot diameter of 30 μm, repetition rate of 5 Hz, and laser fluence of 2 J cm^{-2} were used. Each analysis comprised 20 s of gas-background acquisition followed by 35–40 s of sample-signal acquisition. Zircon 91500 and SA01 were used as the primary and secondary reference materials, respectively. A reference material sequence comprising two analyses of NIST SRM 610, two analyses of zircon 91500, and one analysis of SA01 was conducted after every 7–8 unknown analyses. Data reduction was performed using Iolite software v4 (Elemental Scientific Lasers, Bozeman, MT, USA) [83]. Downhole fractionation was corrected using an exponential function in Iolite [83]. The measured age of SA01 during the analytical session was 542.3 ± 3.5 Ma (2σ), corresponding to a 1.35% deviation from its published reference value of 535.08 ± 0.32 Ma (2σ; [84]).

For each zircon analysis, the best age was taken as the $^{206}Pb/^{238}U$ age for grains younger than 1000 Ma and the $^{207}Pb/^{206}Pb$ age for grains older than 1000 Ma [85]. Analyses with more than 30% discordance or more than 5% reverse discordance were excluded from the detrital zircon age distributions [85]. Concordia diagrams were constructed using Isoplot v3.7 (Berkeley Geochronology Center, Berkeley, CA, USA). Cumulative distribution curves and KDE plots were generated with detritalPy [86]. Zircon U-Pb ages, associated analytical data, and uncertainties at the 2σ level are provided in Supplementary Table S1.

5.2. Kolmogorov–Smirnov Statistical Tests and Multidimensional Scaling

Two-sample Kolmogorov–Smirnov (K-S) tests were used to quantify differences between paired detrital zircon U-Pb age distributions. The null hypothesis states that the two samples were drawn from parent populations with the same age distribution. The K-S

statistic D represents the maximum absolute separation between the empirical cumulative distribution functions of the two samples [87]:

$$D = \sup_x |F_1(x) - F_2(x)| \quad (1)$$

where $F_1(x)$ and $F_2(x)$ are the empirical cumulative distribution functions constructed from the two age datasets. Smaller D values indicate more similar cumulative age distributions, whereas larger D values reflect greater dissimilarity. The corresponding p values were also calculated to assess the statistical significance of each pairwise comparison. A p value greater than 0.05 indicates that the null hypothesis cannot be rejected at the 95% confidence level. However, because K-S p values are sensitive to sample size and may not provide a direct measure of sample similarity, the D values were used as the quantitative dissimilarity measure for subsequent MDS analysis [87]. Pairwise K-S D and p values are listed in Supplementary Table S2.

Although K-S statistics provide a quantitative measure of similarity for each sample pair, the relationships among multiple samples can be more clearly visualized in a multidimensional framework. Multidimensional scaling (MDS) was used to display the relationships among the studied samples and regional reference datasets [88]. The analysis included the six datasets obtained in this study, datasets from modern river sediments in the Qilian Shan and Bei Shan, and the published Silurian datasets DCT-S and NQL-S. Pairwise K-S D values were used as the dissimilarity matrix, and the 3D MDS configuration was generated using DZmds [89]. Each dataset is represented by a point in the MDS configuration. Datasets with similar age distributions plot close together, whereas those with greater differences are separated by larger distances. A Shepard plot was used to compare the original K-S dissimilarities with the distances represented in the MDS configuration. Points close to the 1:1 line indicate close agreement between the original dissimilarities and the fitted MDS distances.

6. Results

6.1. Detrital Zircon U-Pb Age Results

The six samples from Kuantan Shan and adjacent areas comprise three Lower Cretaceous sandstones, one Permian shale, one Carboniferous slate, and one Silurian sandstone. Representative zircon CL images and concordia diagrams are shown in Figure 9. The CL images show internal textures and analytical spots, and the concordia diagrams present the analyses retained according to the concordance criteria. Detrital zircon age distributions and Th/U ratios are shown in Figure 10, and the analytical data are listed in Supplementary Table S1. The Lower Cretaceous quartz arenites yield predominantly Permian and Triassic ages. In contrast, the Permian shale and Carboniferous slate contain Paleozoic and Precambrian age populations. The Silurian quartz arenite is dominated by an early Paleozoic age population.

Zircon grains from Lower Cretaceous sandstone KTS-0728(1), are mostly prismatic to subrounded and range from 50 to 180 μm in size (Figure 9A). Of the 100 grains analyzed, 99 yielded analytical results. Two discordant analyses were excluded, leaving 97 concordant ages (Figure 9A). Th/U ratios range from 0.15 to 1.42 (Figure 10A). The age distribution has two dominant peaks at ca. 243 Ma and ca. 283 Ma, with minor age groups at ca. 419 Ma and ca. 910 Ma. One older grain yielded an age of ca. 1384 Ma. The youngest zircon age is 224.6 ± 2.8 Ma (Figure 10A).

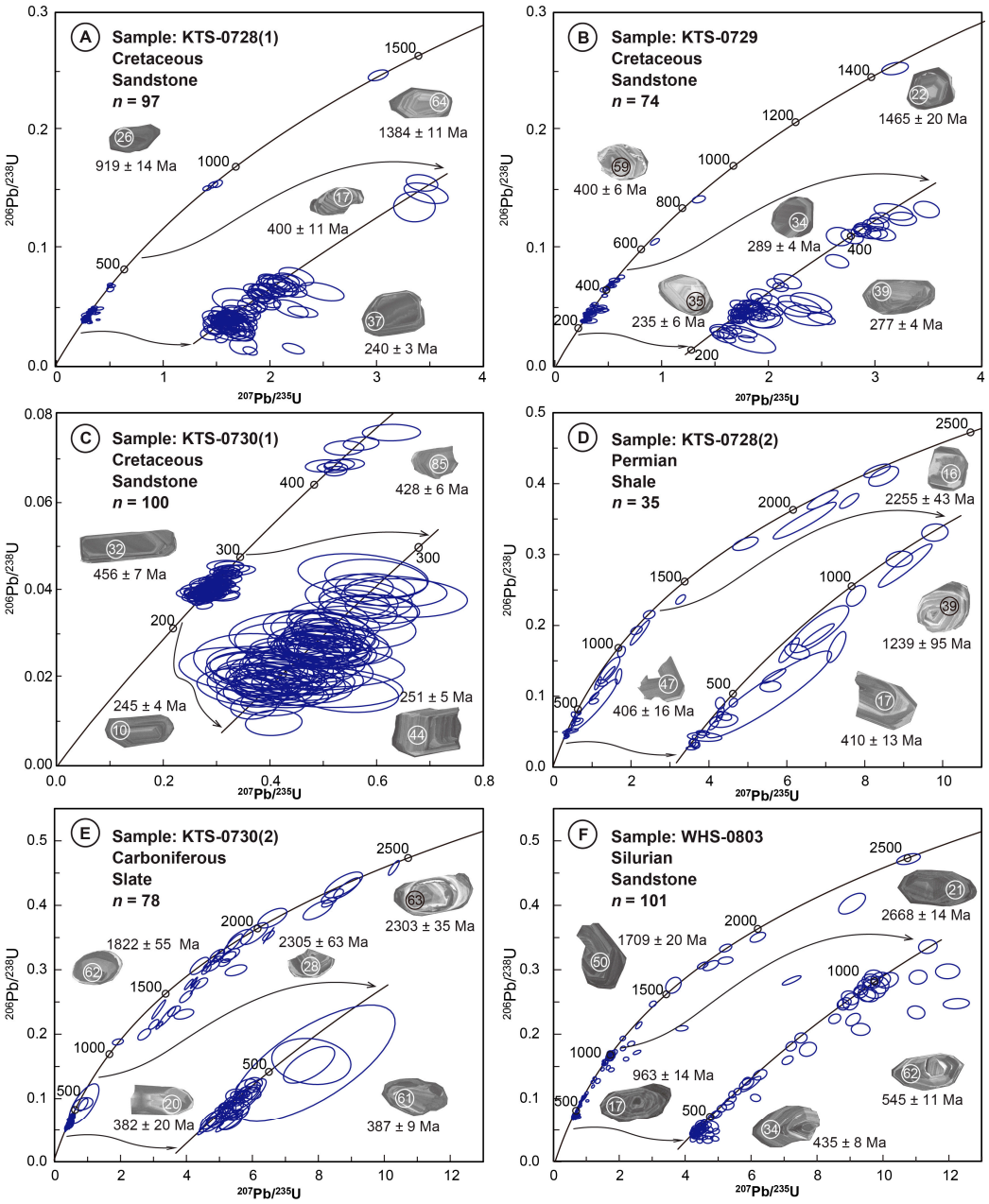


Figure 9. (**A**–**F**) U-Pb concordia diagrams showing zircon age results and representative cathodoluminescence (CL) images of zircon grains for the six analyzed samples. Blue error ellipses represent individual analyses at the 2σ level. The gray curves are concordia curves, with age ticks in Ma. Representative CL images of zircon grains show the locations of the LA–ICP–MS analytical spots. Labels adjacent to the analytical spots report the U–Pb age determined at each spot and its 2σ analytical uncertainty. *n* denotes the number of concordant analyses retained after filtering.

A second Lower Cretaceous sandstone, KTS-0729, contains mostly subrounded to rounded detrital zircons ranging from 40 to 160 μm in size (Figure 9B). Of the 80 grains selected for analysis, 79 yielded analytical results. Five discordant analyses were excluded, leaving 74 concordant ages (Figure 9B). Th/U ratios range from 0.06 to 1.29, with only one value below 0.1 (Figure 10B). The age distribution has a dominant peak at ca. 269 Ma and subordinate age groups at ca. 413 Ma and ca. 235 Ma. A minor age group occurs at ca. 442 Ma. Several older grains yielded ages of ca. 636 Ma, ca. 842 Ma, and ca. 1465 Ma. The youngest zircon age is 228.7 ± 4.8 Ma (Figure 10B).

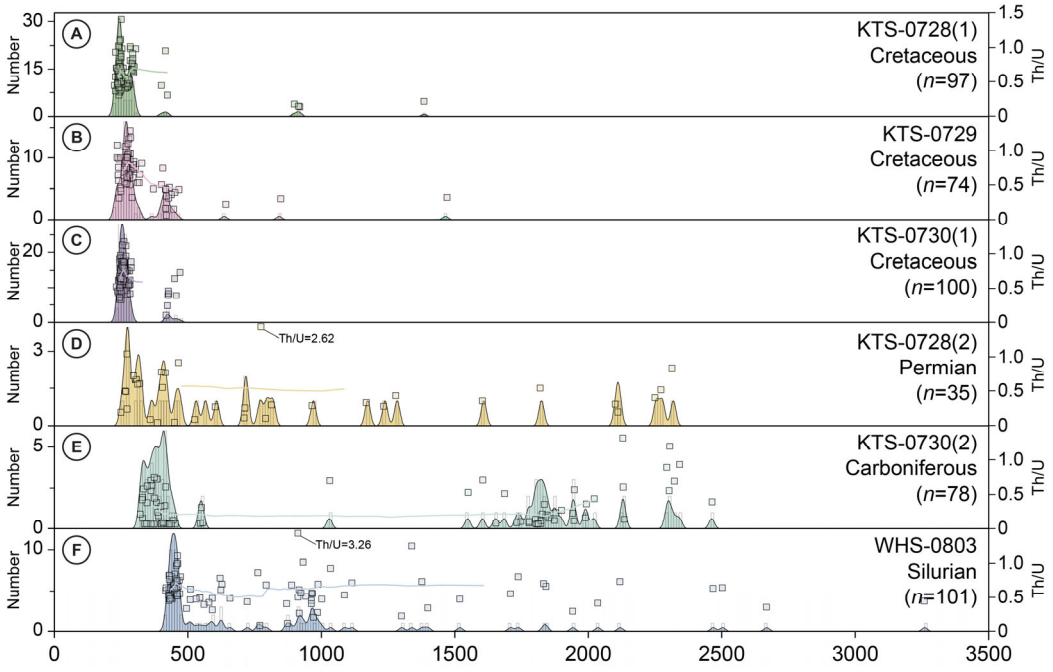


Figure 10. Detrital zircon U-Pb age histograms, probability density plots (PDPs), and Th/U ratios for the six analyzed samples. (**A**) Lower Cretaceous sandstone KTS-0728(1). (**B**) Lower Cretaceous sandstone KTS-0729. (**C**) Lower Cretaceous sandstone KTS-0730(1). (**D**) Permian shale KTS-0728(2). (**E**) Carboniferous slate KTS-0730(2). (**F**) Silurian sandstone WHS-0803. Squares represent Th/U ratios for individual analyses.

Compared with KTS-0729, Lower Cretaceous sandstone KTS-0730(1) yields a more restricted age distribution, dominated by Permian and Triassic ages. Zircon grains are mainly short prismatic, prismatic, and subrounded, with long axes of ca. 50 to 170 μm (Figure 9C). All 100 analyzed grains yielded concordant or nearly concordant ages (Figure 9C). Th/U values fall between 0.10 and 1.17 (Figure 10C). The age distribution is dominated by peaks at ca. 249 Ma and ca. 261 Ma. Subordinate age groups occur at ca. 280 to 283 Ma and ca. 425 Ma. A few older grains yielded ages of ca. 450 to 471 Ma. The youngest zircon age is 232 ± 4 Ma (Figure 10C).

The Permian shale and Carboniferous slate differ from the Cretaceous sandstones in their greater abundance of Precambrian zircons. Detrital zircons from Permian shale KTS-0728(2) are mainly subrounded to rounded, with subordinate short prismatic and euhedral to subhedral grains. Most grains are 40 to 150 μm long (Figure 9D). Of the 50 grains analyzed, 47 yielded analytical results. Twelve discordant analyses were excluded, leaving 35 concordant or nearly concordant ages for further analysis (Figure 9D). Th/U ratios vary from 0.02 to 2.62, with two values below 0.1. The maximum value of 2.62 exceeds the plotted range and is labeled separately in Figure 10D. The retained zircon ages range from 254.3 to 2318.6 Ma. Major Paleozoic age groups occur at ca. 270 to 278 Ma, ca. 311 to 325 Ma, and ca. 392 to 421 Ma. Subordinate groups occur at ca. 455 to 470 Ma, ca. 530 to 608 Ma, and ca. 716 to 819 Ma. Older grains yielded ages of ca. 1174 to 1284 Ma, ca. 1609 to 1825 Ma, and ca. 2106 to 2319 Ma. The youngest zircon age is 254.3 ± 3.2 Ma (Figure 10D).

Detrital zircons from Carboniferous slate KTS-0730(2) records a broad age distribution, with prominent Paleozoic and Precambrian populations. The grains are predominantly subrounded to rounded, although short prismatic and subhedral grains are also present. Most grains are 40 to 140 μm long (Figure 9E). Of the 80 analytical results obtained, 78 were retained following the exclusion of two discordant analyses (Figure 9E). Th/U ratios vary between 0.007 and 1.31, and 27 analyses have values below

0.1 (Figure 10E). The age distribution is dominated by two populations at ca. 380 to 420 Ma and ca. 1800 to 1850 Ma. Subordinate age groups are present at ca. 330 to 350 Ma, ca. 1940 to 1990 Ma, ca. 2130 Ma, and ca. 2300 Ma. A few grains yielded ages of ca. 550 Ma, ca. 1031 Ma, ca. 1550 to 1690 Ma, and ca. 2464 Ma. The youngest grain yielded an age of 321.3 ± 30.8 Ma (Figure 10E).

Unlike the Cretaceous sandstones and the Carboniferous slate, Silurian sandstone WHS-0803 is dominated by early Paleozoic zircons. Most grains are subrounded to rounded, with subordinate short prismatic grains and a few euhedral to subhedral crystals. Their lengths range from 40 to 140 μm (Figure 9F). Analysis of 140 selected grains produced 127 results, of which 101 concordant ages were retained after 26 discordant analyses were rejected (Figure 9F). Th/U ratios lie between 0.07 and 3.26, with most values concentrated between 0.10 and 1.23. Only one analysis has a Th/U ratio below 0.1, and the maximum value of 3.26 is marked separately in Figure 10F. A dominant peak at ca. 447 Ma and a subordinate peak at ca. 960 Ma characterize the age distribution. Minor age groups occur at ca. 595 to 624 Ma, ca. 770 Ma, and ca. 1837 Ma. Older grains have ages of ca. 1300 to 3260 Ma, and the youngest zircon age is 417.4 ± 5.5 Ma (Figure 10F).

6.2. Statistical Results

The statistical comparisons include six new detrital zircon U-Pb datasets from the Kuantan Shan and adjacent areas and four published regional reference datasets (Figures 11 and 12). The six datasets obtained in this study are derived from three Cretaceous sandstone samples, one Permian shale sample, one Carboniferous slate sample, and one Silurian sandstone sample. The published datasets include DCT-S from Early Silurian clastic strata in the Dacaotan area of the North Qilian orogenic belt [90], NQL-S from Silurian strata in the northern Qilian Shan [91], and modern river datasets from the Bei Shan and Qilian Shan [48]. These published datasets provide a regional basis for comparing the detrital zircon age distributions of the studied samples.

6.2.1. KDE and Cumulative Distribution Curves

KDE and cumulative distribution curves were used to compare detrital zircon U-Pb age distributions among the studied samples and regional reference datasets (Figure 11). The cumulative distribution curves show distinct differences between the Cretaceous sandstones and the Paleozoic sedimentary and metasedimentary rocks (Figure 11A). Ages from the three Cretaceous samples, KTS-0728(1), KTS-0729, and KTS-0730(1), are concentrated in a few populations (Figure 11B–D). Their cumulative distribution curves rise steeply between ca. 250 and 450 Ma (Figure 11A). The KDE curves show dominant age populations at ca. 260–300 Ma and subordinate components at ca. 400–450 Ma (Figure 11B–D). Older zircon grains are rare in these samples.

The Permian shale KTS-0728(2) and Carboniferous slate KTS-0730(2) contain a wider range of zircon ages than the Cretaceous sandstones (Figure 11E,F). In KTS-0728(2), several Paleozoic populations occur at ca. 270–278 Ma, ca. 311–325 Ma, and ca. 392–421 Ma. Subordinate age groups are present at ca. 455–470 Ma, ca. 530–608 Ma, and ca. 716–819 Ma (Figure 11E). Older components span ca. 1174–1284 Ma, ca. 1609–1825 Ma, and ca. 2106–2319 Ma. KTS-0730(2) is characterized by prominent Paleozoic populations and a broad older population at ca. 1700–2000 Ma (Figure 11F). Both samples have more gradually rising cumulative distribution curves than the Cretaceous sandstones, consistent with their wider age ranges (Figure 11A).

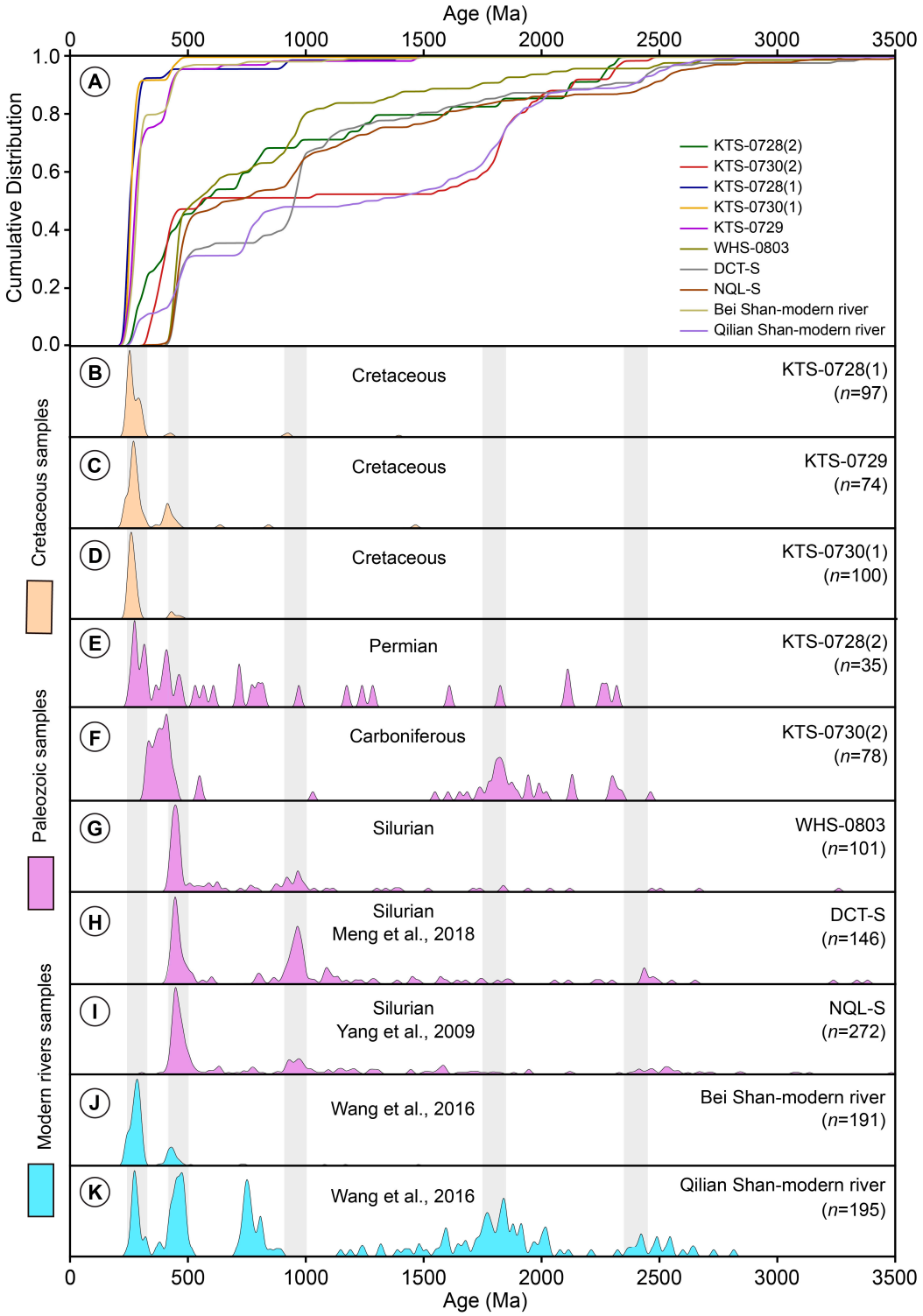


Figure 11. KDE and cumulative distribution curves of detrital zircon U-Pb age distributions between samples from Kuantan Shan and adjacent areas and regional reference datasets. (**A**) Cumulative distribution curves for all datasets. (**B**) Lower Cretaceous sandstone KTS-0728(1). (**C**) Lower Cretaceous sandstone KTS-0729. (**D**) Lower Cretaceous sandstone KTS-0730(1). (**E**) Permian shale KTS-0728(2). (**F**) Carboniferous slate KTS-0730(2). (**G**) Silurian sandstone WHS-0803. (**H**) Published Silurian dataset DCT-S from the Dacaotan area [90]. (**I**) Published Silurian dataset NQL-S from the northern Qilian Shan [91]. (**J**) Modern river-sediment dataset from the Bei Shan [48]. (**K**) Modern river-sediment dataset from the Qilian Shan [48].

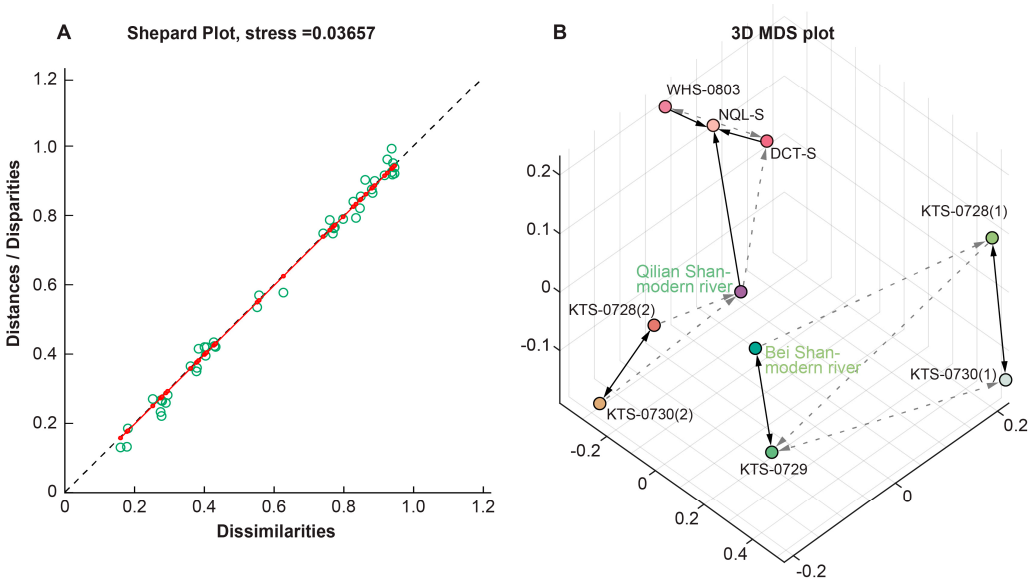


Figure 12. Shepard plot and three-dimensional multidimensional scaling (3D MDS) plot for detrital zircon U-Pb age datasets from the Kuantan Shan and adjacent areas. (**A**) Shepard plot comparing pairwise K–S dissimilarities with interpoint distances in the fitted three-dimensional MDS configuration. (**B**) Three-dimensional MDS configuration derived from the pairwise K–S *D* matrix. Solid and dashed lines connect each dataset to its nearest and second-nearest neighbors, respectively.

An early Paleozoic peak at ca. 450 Ma dominates the age distribution of the Silurian sandstone WHS-0803. Subordinate older components include an age group at ca. 900–1000 Ma (Figure 11G). The published Silurian datasets DCT-S and NQL-S display comparable distributions, with prominent early Paleozoic populations and dispersed older components (Figure 11H,I). In contrast, the Bei Shan modern river dataset is dominated by ages of ca. 260–310 Ma (Figure 11J). Several populations characterize the Qilian Shan modern river dataset, including those at ca. 280 Ma, ca. 430–500 Ma, and ca. 750–950 Ma. Older populations occur at ca. 1700–2000 Ma and ca. 2300–2500 Ma (Figure 11K). These contrasting age spectra provide the basis for the K-S and MDS comparisons in the following section.

6.2.2. Multidimensional Scaling Results

Pairwise K-S *D* and *p* values for the studied samples and reference datasets are listed in Supplementary Table S2. The K-S *D* values were used to construct the dissimilarity matrix for MDS analysis in three dimensions (Figure 12). The Shepard plot compares the original K-S dissimilarities with distances between the datasets in the MDS configuration (Figure 12A). Green open circles represent MDS distances, whereas red circles and the red line show the fitted disparities. The dotted line marks the 1:1 relationship. Most points lie close to this line, showing generally close agreement between the original dissimilarities and the MDS distances.

Links to the nearest and second nearest neighbors show that the three Cretaceous sandstones are more closely associated with the Bei Shan dataset than with the Qilian Shan dataset (Figure 12B). Of these three samples, KTS-0729 lies closest to the Bei Shan modern river dataset. KTS-0728(1) and KTS-0730(1) are nearest neighbors, and their links to second nearest neighbors extend toward the part of the configuration occupied by the Cretaceous samples and the Bei Shan dataset. These spatial relationships indicate greater similarity between the zircon age distributions of the Cretaceous sandstones and the Bei Shan reference dataset.

By contrast, the Permian shale KTS-0728(2), Carboniferous slate KTS-0730(2), and Silurian sandstone WHS-0803 instead plot closer to the Qilian Shan reference datasets (Figure 12B). KTS-0728(2) and KTS-0730(2) form a pair of nearest neighbors, with links to second nearest neighbors toward the Qilian Shan modern river dataset. WHS-0803 lies close to the published Silurian datasets DCT-S and NQL-S, of which NQL-S is its nearest neighbor. The MDS configuration thus distinguishes two groups among the studied samples. The Cretaceous sandstones show greater similarity to the Bei Shan dataset, whereas the Paleozoic samples are more closely associated with the Qilian Shan datasets.

7. Discussion

7.1. Structural Evidence for the Kuantan Shan Thrust and Nappe System

Regional thrust and nappe systems are recognized by laterally extensive basal thrusts, tectonic juxtaposition or repetition of stratigraphic units, and fault-related folds [92–94]. Where erosion dissects a formerly continuous thrust sheet, isolated erosional remnants form klippen [75,95]. A gently dipping basal thrust that places older rocks above younger strata provides important evidence for recognizing a thrust klippe [75]. In the central Himalaya, the Damauli klippe has been interpreted as a remnant of a thrust sheet that formerly extended between the Kathmandu and Jajarkot klippen, based on its tectonosedimentary setting [96]. The Klippen nappe in the Swiss Prealps provides a well-documented example of an integrated nappe system in which a basal detachment, internal stratigraphic succession, imbricate thrusts, associated folds, and klippen collectively define the regional structural architecture [92,97,98]. In the northern Qilian Shan, previous work [33] defined a regional thrust and nappe system comprising the NQT root belt, intervening thrust slices and small klippen, and the frontal Yumu Shan klippe. This regional framework provides a basis for evaluating the thrust faults, associated folds, and isolated Paleozoic bodies exposed at Kuantan Shan.

Surface structures at Kuantan Shan and regional seismic reflection profiles define an imbricate thrust system with northward vergence. The NQT marks the root zone of the system, whereas the NKTF forms the basal thrust beneath the frontal klippen. Along the NQT, Silurian strata are thrust over the Chijinpu Formation, which is tightly folded in the footwall (Figure 5E). Farther north, the NKTF dips gently southward and places Cambrian schist above the Chijinpu Formation (Figure 5). The isolated Cambrian bodies west of the main Kuantan Shan massif are interpreted as erosional remnants of the frontal thrust sheet. Beneath the NKTF, the Chijinpu Formation displays pronounced bedding deflection and local overturning (Figure 6). Similar footwall drag folds have been documented beneath other thrusts [99]. These structural relationships and the footwall drag folds indicate northward thrusting from the northern Qilian Shan toward the Hexi Corridor (Figures 5 and 6).

This interpretation is consistent with the regional architecture of the North Qilian thrust and nappe system. Previous studies [32,33] divided this system into root, middle, and frontal belts. The NQT forms the root belt, isolated klippen occur within the middle belt, and the Yumu Shan klippe occupies the frontal belt. The Kuantan Shan klippen occur in comparable structural positions between the NQT and the Hexi Corridor and may represent the western continuation of this Early Cretaceous thrust and nappe system. Growth strata in the Lower Cretaceous succession at Kuantan Shan independently indicate that folding accompanied sedimentation. Comparable growth strata associated with Early Cretaceous thrusting have been documented at Liyuanpu and Yumu Shan [18,33]. These relationships support an Early Cretaceous age for the principal nappe emplacement.

Deep seismic reflection profiles image thrusts that dip south and verge north beneath the transition between the northern Qilian Shan and the Hexi Corridor. Their geometry in the upper crust is consistent with the thrust structures exposed at Kuantan Shan. Continuous

Jurassic and Cretaceous reflectors in the foreland are progressively folded and truncated toward the range front [82]. A frontal thrust carries Cretaceous strata over the subhorizontal Mesozoic and Cenozoic succession. A thrust farther into the hinterland cuts the hanging wall of the frontal thrust and places Ordovician and Silurian rocks above Cretaceous strata (Figure 8). These thrusts merge downward into an intracrustal detachment at depths of 14 to 24 km [100]. The regional seismic geometry suggests that the Kuantan Shan thrust and nappe system may be linked at depth to the intracrustal detachment.

7.2. Detrital Zircon U-Pb Evidence for Provenance Contrast Across the Kuantan Shan Thrust and Nappe System

The Lower Cretaceous footwall sandstones (KTS-0728(1), KTS-0729, and KTS-0730(1)) contain abundant detrital zircons with ages of ca. 240 to 320 Ma, with dominant peaks at ca. 260 to 300 Ma and subordinate early Paleozoic grains at ca. 400 to 450 Ma (Figure 11B–D). Granitic plutons with ages of ca. 230 to 310 Ma are exposed in the Bei Shan and provide potential sources for the dominant zircon population. However, Permian and Triassic plutons also occur in the Qilian Shan, so these ages alone do not distinguish the two source regions [18,34]. The dominance of late Paleozoic zircons and scarcity of Precambrian grains in the footwall sandstones resemble the age distributions reported from the northern Yumen Basin. The northern Yumen sandstones contain predominantly ca. 240 to 290 Ma zircons and were interpreted to have been sourced mainly from the Bei Shan [34]. The KDE curves for the three Cretaceous sandstone samples from Kuantan Shan and cumulative age distributions also resemble the Bei Shan reference spectrum, and they plot closer to the Bei Shan modern river dataset than to the Qilian Shan dataset in the MDS diagram (Figure 11J,K and Figure 13B). These comparisons suggest an important Bei Shan contribution to the Lower Cretaceous sandstones at Kuantan Shan.

Regional provenance studies indicate that Cretaceous sediment sources varied across the Hexi Corridor. The northern Yumen Basin received sediment mainly from the Bei Shan, whereas the westernmost Yumen Basin records contributions from both the Bei Shan and Qilian Shan [34]. At Liyuanpu, detrital zircon ages and published paleocurrent data indicate sediment supply from both the Qilian Shan and Longshou Shan [18]. In the Pingshanhu Basin, zircon age distributions and paleocurrent data indicate an Alxa source for the lower Miaogou Group. The upper Miaogou Group records contributions from both the Alxa block and northern Qilian Shan [19]. These records indicate that sediment supply from the northern and southern margins of the Hexi Corridor varied among basins and through time. At Kuantan Shan in the western Hexi Corridor, the zircon age spectra indicate an important Bei Shan contribution to the Lower Cretaceous deposits (Figures 10 and 11B–D).

The Paleozoic hanging wall samples KTS-0728(2) and KTS-0730(2) contain early Paleozoic and Precambrian zircon populations. Similar populations occur in the regional Silurian sample WHS-0803 but are poorly represented in the Cretaceous footwall samples (Figure 11E–G). The ca. 435 to 500 Ma population is generally associated with Cambrian and Ordovician subduction and arc magmatism, followed by ocean closure and continental collision. These processes are recorded by ophiolitic mélanges, igneous rocks associated with arc magmatism, high pressure metamorphic rocks, Silurian flysch, and post collisional sedimentary successions across the Qilian Orogen [15,17,36,38–42,91,101,102]. Older populations occur at ca. 950 to 1050 Ma, 1750 to 1850 Ma, and 2350 to 2550 Ma. These populations are commonly interpreted as recycled material from the Archean and Proterozoic basement of the Qilian Orogen and adjacent cratonic domains [15,17,36,91,103]. The association of early Paleozoic and Precambrian populations resembles the zircon age distributions of regional Paleozoic strata associated with the Qilian Orogen. These age distributions differ from those of the Cretaceous footwall samples, which are dominated by Permian zircons.

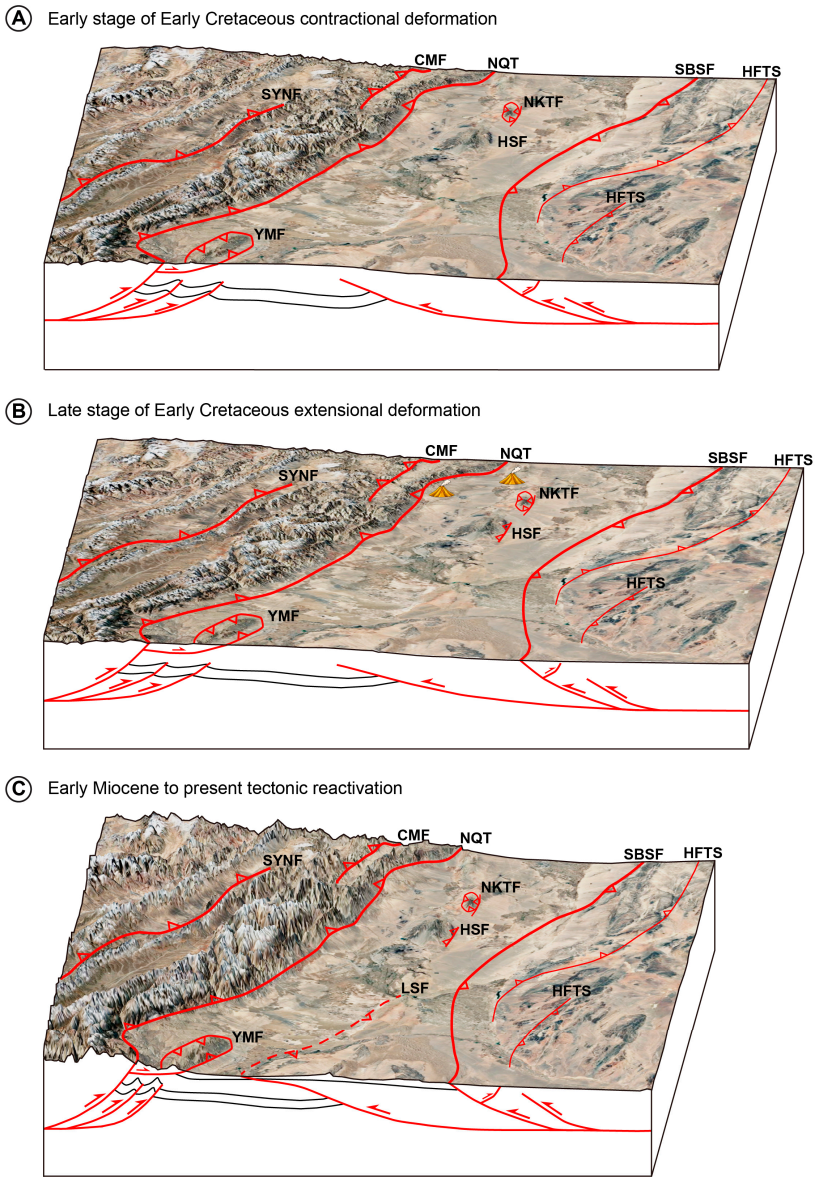


Figure 13. Three-stage tectonic evolution model of the northern margin of the Qilian Shan, the Hexi Corridor, and the Beishan region since the Early Cretaceous. The topographic base was constructed by draping Google Earth imagery over the Copernicus DEM GLO-30. Regional fault traces were generalized from [12,64], whereas the Kuantan Shan thrust and nappe system is based on this study. SYNF-South Yeniugou fault; YMF-Yumushan fault; CMF-Changma fault; NQT-North Qilian Thrust; NKTF-North Kuantanshan thrust fault; HSF-Hongshan fault; LSF-Longshoushan fault; SBSF-Shibanshan fault; HFTS-Hongliudaquan fold-and-thrust system.

Comparison with regional Silurian strata further supports this affinity. The DCT-S dataset from Dacaotan contains major age groups at 434 to 521 Ma, 791 to 992 Ma, 1017 to 1755 Ma, and 1879 to 2663 Ma. The early Paleozoic, Neoproterozoic, and older basement components in these Early Silurian clastic rocks were interpreted to record important sediment contributions from the Qilian Orogen [90]. The NQL-S dataset from Silurian strata in the northern Qilian Shan likewise records early Paleozoic magmatic sources together with Proterozoic and Archean detritus [91]. In the MDS diagram, WHS-0803 plots close to DCT-S and NQL-S. The Paleozoic hanging wall samples also plot closer to the Qilian Shan reference datasets than to the Bei Shan modern river dataset (Figure 12B). The statistical comparisons and MDS analysis therefore support similarities among these age distributions, rather than only a correspondence between individual age peaks. These relationships

indicate a stronger provenance affinity with the Qilian Orogen for the Paleozoic hanging wall strata than for the Lower Cretaceous footwall strata.

The detrital zircon data provide an independent basis for distinguishing the Lower Cretaceous basin fill from the Paleozoic hanging wall rocks. The footwall sandstones are dominated by Permian zircons and show greater similarity to the Bei Shan reference datasets. In contrast, the Paleozoic hanging wall samples contain early Paleozoic and Precambrian zircon populations (Figures 10 and 11B–G). These populations are comparable to those reported from Silurian strata in the northern Qilian Shan [91]. Previous studies in the Hexi Corridor and the Yumen and Jiuxi basins have collectively used detrital zircon ages, sandstone compositions, sedimentologic observations, paleocurrent data, thermochronology, and structural relationships to distinguish sediment derived from the Bei Shan and Qilian Shan [12,25,28,34,45–48,53,104–108]. At Kuantan Shan, the NKTF places Paleozoic strata with a Qilian affinity above the Lower Cretaceous Chijinpu Formation, whose detrital zircon record indicates an important Bei Shan contribution (Figures 5, 6, 10 and 11B). These relationships indicate that the Paleozoic hanging wall rocks constitute a tectonostratigraphic slice within the Kuantan Shan thrust and nappe system.

7.3. Tectonic Evolution of the Northern Tibetan Plateau Since the Early Cretaceous

The structural record at Kuantan Shan constrains the geometry, transport direction, and timing of the thrust and nappe system. In its southern root zone, the NQT places Middle Silurian strata above the Lower Cretaceous Chijinpu Formation, whose footwall contains tight fault-related folds (Figure 5E). Farther north, the NKTF has an attitude of 148°/20° (dip direction/dip angle) and places Cambrian schist above the Chijinpu Formation (Figure 5A–D). The isolated Cambrian bodies west of the main Kuantan Shan massif are interpreted as klippen derived from the same frontal thrust sheet. Progressive bedding deflection and local overturning beneath the NKTF define footwall drag folds and support northward tectonic transport (Figure 6). Within the Growth strata interval, beds adjacent to the thrust dip 80–85° south, whereas beds farther northeast dip north and progressively shallow from 78° to approximately 20° (Figure 7B–D). Seven bedding poles define a best-fit great circle with a subhorizontal, approximately E–W π axis (Figure 7B). The Growth strata constrain folding and thrusting to the earlier part of the Early Cretaceous. Detrital zircon age spectra distinguish the Paleozoic allochthon of Qilian affinity from the Lower Cretaceous footwall, supporting the tectonic juxtaposition of two distinct tectonostratigraphic units.

Comparable growth strata and Early Cretaceous contractional structures at Yumu Shan, Liyuanpu, and Pingshanhu extend this deformation record across the northern Qilian Shan, Hexi Corridor, and southern Bei Shan [18,19,32,33]. Regional seismic reflection profile images north-vergent imbricate and blind thrusts that merge downward into intracrustal detachments and record shortening in the upper crust [82,100]. These profiles provide a crustal-scale framework for the surface structures. Regional studies provide the temporal context for interpreting this seismic profile. Previous studies [32,33] interpreted the Yumu Shan thrust and nappe system associated with the NQT to the early stage of the Early Cretaceous. They also recognized local reactivation during Cenozoic shortening. Likewise, Paleocene to Eocene deformation across northern Tibet preferentially reactivated Cretaceous structures [109]. Early Cretaceous folding followed by late Miocene deformation has also been documented at Liyuanpu [18]. This contraction broadly coincided with the terminal evolution of the Bangong Nujiang Ocean and continued convergence between the Lhasa and Qiangtang terranes. Their temporal correspondence supports northward transmission of compressional stress from the Tethyan orogenic system [110–114]. Spatial variations in shortening kinematics across the Bei Shan indicate that inherited crustal structures partitioned this far field stress. Tectonic forcing from the Mongol Okhotsk and Paleo Pacific

domains may also have contributed to this deformation [64,115–118]. The temporal and spatial correspondence of these contractional records favors their interpretation as a far field response to convergence between the Lhasa and Qiangtang terranes, rather than an isolated deformation event in the western Hexi Corridor (Figure 13A).

Following Early Cretaceous thrusting, the northern Qilian Shan and Hexi Corridor underwent regional extension during the late Early Cretaceous. Near Kuantan Shan, this transition is recorded by coeval mafic magmatism along the southern margin of the Jiuxi Basin (Figure 13B). At Hanxia, mafic volcanic rocks are interbedded with the Xiagou Formation [119]. At Hongliuxia, a volcanic neck and associated lava flows record Cretaceous volcanic activity [50]. K–Ar ages of ca. 119 to 107 Ma constrain this magmatism to the late Early Cretaceous [50,120]. The alkaline to shoshonitic affinities and geochemical signatures of an enriched mantle source have been interpreted to reflect magmatism in a continental extensional setting [119]. Within the Jiuxi Basin, differential activity along the northeastern boundary fault of the Qingxi Sag controlled migration of the Xiagou Formation depocenters. Basin subsidence subsequently changed from strongly fault-controlled subsidence to more uniform subsidence [51]. Eastward, the north dipping Hongshan normal fault postdates Early Cretaceous folding in the Liyuanpu area [18]. Balanced cross-section restoration indicates 2.08 km of extension in the Pingshanhu Basin, whereas the Lower Cretaceous successions of the Minle and Chaoshui basins preserve normal faults and synsedimentary stratal rotation [10,19]. The association of normal faulting, fault-controlled subsidence, and mafic magmatism indicates a regional transition from contraction to extension across the Hexi Corridor (Figure 13B). This transition may reflect gravitational collapse of crust thickened during the preceding contraction [18,33,121].

Cenozoic contraction subsequently reactivated and modified this Mesozoic structural framework in response to India–Eurasia convergence [27,28,122]. At Kuantan Shan and Hei Shan, apatite fission track data and thermal history modeling record renewed cooling and exhumation during the Eocene and since the middle Miocene [27]. Along the northern margin of the Jiuxi Basin, the Eocene Huoshaogou Formation contains poorly sorted conglomerates with angular to subangular clasts. Together with southward paleocurrents and detrital zircon evidence for northern sources, these deposits indicate erosion of nearby uplands during the early Cenozoic [28]. Seismic interpretation and balanced section restoration across the Kuantan Shan and Hei Shan area reveal steep faults involving the basement and positive flower structures, with approximately 2.2 km of Cenozoic shortening along the restored section [28]. Farther east, Miocene cooling in the northern Qilian Shan and Longshou Shan has been related to renewed activity along the NQT and Longshou Shan thrust [122]. Broad, gentle folds in Miocene strata at Liyuanpu and Cenozoic folding and thrusting around Yumu Shan record renewed shortening superimposed on the earlier Cretaceous structures [18,33]. These regional records indicate that Cenozoic contraction reactivated inherited faults and further deformed the Mesozoic successions. The present configuration of basins and ranges thus records Early Cretaceous thrusting, late Early Cretaceous extension, and Cenozoic reactivation accompanied by renewed shortening and exhumation (Figure 13C).

8. Conclusions

Field observations, growth strata, detrital zircon U–Pb age spectra, and the regional seismic reflection profile provide complementary evidence for the Early Cretaceous thrust system at Kuantan Shan. Together, these data constrain its surface and subsurface geometry, transport direction, stratigraphic provenance, and relation to Early Cretaceous contraction and extension along the northern Qilian Shan and Hexi Corridor, as well as its subsequent modification during Cenozoic deformation.

(1) Field relationships and the regional seismic reflection profile define a thrust and nappe system with northward vergence at Kuantan Shan. The NQT dips south and forms the root zone of the system. Farther north, the gently dipping NKTF forms the basal contact beneath Paleozoic klippen that structurally overlie the Lower Cretaceous Chijinpu Formation. Drag deformation in the footwall of the NKTF records tectonic transport toward the Hexi Corridor. The regional seismic profile show imbricate and blind thrusts that dip south and merge downward into an intracrustal detachment. These structures define an integrated system of upper-crustal shortening with northward tectonic transport.

(2) Detrital zircon U-Pb ages indicate distinct source regions for the Lower Cretaceous footwall strata and the Paleozoic allochthon. Sandstones in the footwall are dominated by Permian zircon populations and show a closer affinity to sources in the Beishan. The allochthon contains abundant Early Paleozoic and Precambrian zircon populations characteristic of the Qilian Shan. Its Qilian provenance and structural position above the Lower Cretaceous basin succession record northward transport of a Paleozoic thrust sheet into the Hexi Corridor.

(3) During the early stage of the Early Cretaceous, northward thrusting at Kuantan Shan formed part of a regional episode of shortening along the northern Qilian Shan and Hexi Corridor. Contemporaneous contraction is recorded by thrust faults and growth strata at Yumu Shan, Liyuanpu, and the Pingshanhu Basin. This deformation broadly coincided with the terminal evolution of the Bangong Nujiang Ocean and continued convergence between the Lhasa and Qiangtang terranes. The Kuantan Shan thrust and nappe system is therefore interpreted as a distant response to this convergence. Normal faulting and mafic magmatism record a subsequent phase of extension during the late Early Cretaceous. Later Cenozoic shortening reactivated the NQT and LSF and contributed to the present structural configuration.

Supplementary Materials: The following supporting information can be downloaded at https://www.mdpi.com/article/10.3390/min16111195/s1, Table S1: LA-ICP-MS U-Pb isotopic data for detrital zircons from the Kuantan Shan and adjacent areas; Table S2: Two-sample Kolmogorov–Smirnov test results for detrital zircon U-Pb age distributions of the studied samples and regional reference datasets.

Author Contributions: Conceptualization: Y.D., Z.S. and B.L.; Methodology: Y.D., B.L. and X.C.; Software: Y.D.; Validation: Y.D. and X.C.; Formal analysis: Y.D.; Investigation: Y.D. and D.X.; Resources: Y.D., B.L. and D.X.; Data curation: Y.D., D.X. and L.H.; Writing—original draft: Y.D.; Writing—review & editing: Y.D., Z.S., B.L. and X.C.; Visualization: Y.D.; Supervision: Z.S., B.L., X.C. and L.H.; Project administration: Z.S., B.L., D.X. and L.H.; Funding acquisition: Z.S. and B.L. All authors have read and agreed to the published version of the manuscript.

Funding: This research was funded by Deep Earth Probe and Mineral Resources Exploration-National Science and Technology Major Project, grant number 2024ZD1000100 and Deep Earth Probe and Mineral Resources Exploration-National Science and Technology Major Project, grant number 2024ZD1000103.

Data Availability Statement: Data are available on request from the authors. The data are not publicly available due to their inclusion in an ongoing doctoral dissertation that has not yet been completed.

Conflicts of Interest: The authors declare no conflict of interest.

References

1. Yin, A.; Harrison, T.M. Geologic evolution of the Himalayan–Tibetan orogen. *Annu. Rev. Earth Planet. Sci.* **2000**, *28*, 211–280. [CrossRef]

2. Tapponnier, P.; Xu, Z.; Roger, F.; Meyer, B.; Arnaud, N.; Wittlinger, G.; Yang, J. Oblique stepwise rise and growth of the Tibet Plateau. *Science* **2001**, *294*, 1671–1677. [CrossRef]
3. Royden, L.H.; Burchfiel, B.C.; van der Hilst, R.D. The geological evolution of the Tibetan Plateau. *Science* **2008**, *321*, 1054–1058. [CrossRef]
4. Yin, A. Cenozoic tectonic evolution of Asia: A preliminary synthesis. *Tectonophysics* **2010**, *488*, 293–325. [CrossRef]
5. Clark, M.K. Continental collision slowing due to viscous mantle lithosphere rather than topography. *Nature* **2012**, *483*, 74–77. [CrossRef]
6. Ma, X.; Dai, S.; Zhang, Z.; Wang, R.; Wang, Z.; Fan, X.; Ding, Z.; Yang, J.; Ma, H.; Ji, T.; et al. Early Oligocene onset of the Qilian Shan uplift in the northeastern Tibetan Plateau: Evidence from magnetostratigraphy and provenance from the Jiuxi Basin. *Tectonics* **2025**, *44*, e2025TC008864. [CrossRef]
7. He, Z.; Wang, H.; Song, S.; Wang, Z.; Xiong, Z.; Shen, X.; Glorie, S.; Liang, Y.; Zhong, L.; De Grave, J. Late Eocene to Oligocene intracontinental deformation and growth of the northwestern Tibetan Plateau. *Commun. Earth Environ.* **2026**, *7*, 560. [CrossRef]
8. Molnar, P.; Tapponnier, P. Cenozoic tectonics of Asia: Effects of a continental collision. *Science* **1975**, *189*, 419–426. [CrossRef]
9. Li, B.; Zuza, A.V.; Chen, X.; Hu, D.; Shao, Z.; Qi, B.; Wang, Z.; Levy, D.A.; Xiong, X. Cenozoic multi-phase deformation in the Qilian Shan and out-of-sequence development of the northern Tibetan Plateau. *Tectonophysics* **2020**, *782–783*, 228423. [CrossRef]
10. Vincent, S.J.; Allen, M.B. Evolution of the Minle and Chaoshui basins, China: Implications for Mesozoic strike-slip basin formation in Central Asia. *Geol. Soc. Am. Bull.* **1999**, *111*, 725–742. [CrossRef]
11. Chen, X.H.; Yin, A.; Gehrels, G.E.; Cowgill, E.S.; Grove, M.; Harrison, T.M.; Wang, X.F. Two phases of Mesozoic north-south extension in the eastern Altyn Tagh range, northern Tibetan Plateau. *Tectonics* **2003**, *22*, 1053. [CrossRef]
12. Chen, X.H.; Shao, Z.G.; Xiong, X.S.; Gao, R.; Liu, X.J.; Wang, C.F.; Li, B.; Wang, Z.Z.; Zhang, Y.P. Fault system, deep structure and tectonic evolution of the Qilian Orogenic Belt, Northwest China. *Geol. China* **2019**, *46*, 995–1020. [CrossRef]
13. Yin, A.; Dang, Y.-Q.; Wang, L.-C.; Jiang, W.-M.; Zhou, S.-P.; Chen, X.-H.; Gehrels, G.E.; McRivette, M.W. Cenozoic tectonic evolution of Qaidam basin and its surrounding regions (Part 1): The southern Qilian Shan–Nan Shan thrust belt and northern Qaidam basin. *Geol. Soc. Am. Bull.* **2008**, *120*, 813–846. [CrossRef]
14. Yin, A.; Dang, Y.-Q.; Zhang, M.; Chen, X.-H.; McRivette, M.W. Cenozoic tectonic evolution of Qaidam basin and its surrounding regions (Part 3): Structural geology, sedimentation, and regional tectonic reconstruction. *Geol. Soc. Am. Bull.* **2008**, *120*, 847–876. [CrossRef]
15. Gong, H.; Zhao, H.; Xie, W.; Kang, W.; Zhang, R.; Yang, L.; Zhang, Y.; Song, J.; Zhang, Y. Tectono-thermal events of the North Qilian Orogenic Belt, NW China: Constraints from detrital zircon U–Pb ages of Heihe River sediments. *J. Asian Earth Sci.* **2017**, *138*, 647–656. [CrossRef]
16. Zuza, A.V.; Wu, C.; Reith, R.C.; Yin, A.; Li, J.; Zhang, J.Y.; Zhang, Y.X.; Wu, L.; Liu, W. Tectonic evolution of the Qilian Shan: An early Paleozoic orogen reactivated in the Cenozoic. *Geol. Soc. Am. Bull.* **2018**, *130*, 881–925. [CrossRef]
17. Li, B.; Zuza, A.V.; Chen, X.; Wang, Z.; Shao, Z.; Levy, D.A.; Wu, C.; Xu, S.; Sun, Y. Pre-Cenozoic evolution of the northern Qilian Orogen from zircon geochronology: Framework for early growth of the northern Tibetan Plateau. *Palaeogeogr. Palaeoclimatol. Palaeoecol.* **2021**, *562*, 110091. [CrossRef]
18. Wang, Y.; Chen, X.H.; Zhang, Y.Y.; Yin, Z.; Zuza, A.V.; Yin, A.; Wang, Y.C.; Ding, W.C.; Xu, S.L.; Zhang, Y.P.; et al. Superposition of Cretaceous and Cenozoic deformation in northern Tibet: A far-field response to the tectonic evolution of the Tethyan orogenic system. *Geol. Soc. Am. Bull.* **2022**, *134*, 501–525. [CrossRef]
19. Liu, W.; Wu, C.; Li, J.; Zhang, C.; Jiang, T.; Zuza, A.V.; Haproff, P.J.; Chen, X.; Yue, Y. Structure and provenance of the Cretaceous Pingshanhu Basin in the Hexi Corridor: Implications for Mesozoic tectonics in the northern Tibetan Plateau. *Geosphere* **2024**, *20*, 421–450. [CrossRef]
20. He, Z.; Glorie, S.; Boutsalis, C.; Jolivet, M.; Nixon, A.; De Grave, J. Thermo-tectonic history of the Qilian Shan and adjacent areas: New insights from apatite U-Pb and fission track thermochronology. *Tectonics* **2025**, *44*, e2024TC008407. [CrossRef]
21. Ma, X.; Dai, S.; Zhang, Z.; Wang, R.; Ji, T.; Ding, Z.; Qiao, Q. Meso-Cenozoic tectonic deformation of the Qilian Shan, northeastern Tibetan Plateau: Insights from detrital apatite fission-track analysis in the Jiuquan Basin. *Palaeogeogr. Palaeoclimatol. Palaeoecol.* **2026**, *696*, 113882. [CrossRef]
22. George, A.D.; Marshallsea, S.J.; Wyrwoll, K.-H.; Chen, J.; Lu, Y.C. Miocene cooling in the northern Qilian Shan, northeastern margin of the Tibetan Plateau, revealed by apatite fission-track and vitrinite-reflectance analysis. *Geology* **2001**, *29*, 939–942. [CrossRef]
23. Duvall, A.R.; Clark, M.K.; Pluijm, B.A.V.D.; Li, C. Direct dating of Eocene reverse faulting in northeastern Tibet using Ar-dating of fault clays and low-temperature thermochronometry. *Earth Planet. Sci. Lett.* **2011**, *304*, 520–526. [CrossRef]
24. Yuan, D.Y.; Ge, W.P.; Chen, Z.W.; Li, C.Y.; Wang, Z.C.; Zhang, H.P.; Zhang, P.Z.; Zheng, D.W.; Bi, W.J.; Craddock, W.H.; et al. The growth of northeastern Tibet and its relevance to large-scale continental geodynamics: A review of recent studies. *Tectonics* **2013**, *32*, 1358–1370. [CrossRef]

25. Zheng, D.W.; Wang, W.T.; Wan, J.L.; Yuan, D.Y.; Liu, C.C.; Zheng, W.J.; Zhang, H.P.; Pang, J.Z.; Zhang, P.Z. Progressive northward growth of the northern Qilian Shan-Hexi Corridor (northeastern Tibet) during the Cenozoic. *Lithosphere* **2017**, *9*, 408–416. [CrossRef]
26. Yu, J.X.; Pang, J.Z.; Wang, Y.Z.; Zheng, D.W.; Liu, C.C.; Wang, W.T.; Li, Y.; Li, C.; Xiao, L. Mid-Miocene uplift of the northern Qilian Shan as a result of the northward growth of the northern Tibetan Plateau. *Geosphere* **2019**, *15*, 423–432. [CrossRef]
27. An, K.; Lin, X.; Wu, L.; Yang, R.; Chen, H.; Cheng, X.; Xia, Q.; Zhang, F.; Ding, W.; Gao, S.; et al. An immediate response to the Indian–Eurasian collision along the northeastern Tibetan Plateau: Evidence from apatite fission track analysis in the Kuantan Shan–Hei Shan. *Tectonophysics* **2020**, *774*, 228278. [CrossRef]
28. An, K.; Lin, X.; Huang, J.; Wu, L.; Chen, H.; Cheng, X.; Li, C.; Chen, Y.; Wang, Z. Early Cenozoic Reactivation of a Pre-Existing Crustal Boundary Along the Kuantan Shan-Hei Shan Area North of the Jiuxi Basin, Northeastern Tibetan Plateau. *Tectonics* **2025**, *44*, e2024TC008615. [CrossRef]
29. Balansa, J.; Espurt, N.; Hippolyte, J.-C.; Philip, J.; Caritg, S. Structural evolution of the superimposed Provençal and Subalpine fold-thrust belts (SE France). *Earth-Sci. Rev.* **2022**, *227*, 103972. [CrossRef]
30. Sanità, E.; Lardeaux, J.-M.; Marroni, M.; Pandolfi, L. Kinematics of the Helminthoid Flysch–Marguareis Unit tectonic coupling: Consequences for the tectonic evolution of Western Ligurian Alps. *Comptes Rendus Géosci.* **2022**, *354*, 141–157. [CrossRef]
31. Sanità, E.; Lardeaux, J.-M.; Pandolfi, L. Multiphase tectonic evolution of the Maritime–Ligurian Alps transition zone (SW Alps): Insights from an integrated multidisciplinary dataset. *J. Struct. Geol.* **2026**, *205*, 105637. [CrossRef]
32. Chen, X.H.; Shao, Z.G.; Xiong, X.S.; Gao, R.; Xu, S.L.; Zhang, Y.P.; Li, B.; Wang, Y. Early Cretaceous overthrusting of Yumu Mountain and hydrocarbon prospect on the northern margin of the Qilian orogenic belt. *Acta Geosci. Sin.* **2019**, *40*, 377–392. [CrossRef]
33. Han, L.; Ding, W.; Chen, X.; Shao, Z.; Zhang, D.; Xiao, Y.; He, C.; Wang, Z.; Li, B.; Zhang, Y.; et al. Early Cretaceous thrust and nappe tectonics in North Qilian Shan, northern Tibetan Plateau: Evidence from field mapping, geochronology, and deep structural analysis. *Acta Geol. Sin. (Engl. Ed.)* **2023**, *97*, 1058–1077. [CrossRef]
34. Cheng, F.; Garzione, C.N.; Jolivet, M.; Wang, W.; Dong, J.; Richter, F.; Guo, Z. Provenance analysis of the Yumen Basin and northern Qilian Shan: Implications for the pre-collisional paleogeography in the NE Tibetan plateau and eastern termination of Altyn Tagh fault. *Gondwana Res.* **2019**, *65*, 156–171. [CrossRef]
35. Li, J.; Wu, C.; Li, X.; Zuza, A.V.; Haproff, P.J.; Zhao, Y.; Zhao, W.; Yue, Y.; Ding, L. Tectonic inversion of an intracontinental rift basin: An example from the opening and closure of the Paleo-Tethys Ocean, northern Tibetan Plateau. *Geol. Soc. Am. Bull.* **2024**, *136*, 5145–5173. [CrossRef]
36. Wu, C.; Zuza, A.V.; Yin, A.; Liu, C.F.; Reith, R.C.; Zhang, J.Y.; Liu, W.C.; Zhou, Z.G. Geochronology and geochemistry of Neoproterozoic granitoids in the central Qilian Shan of northern Tibet: Reconstructing the amalgamation processes and tectonic history of Asia. *Lithosphere* **2017**, *9*, 609–636. [CrossRef]
37. Xiao, W.J.; Mao, Q.G.; Windley, B.F.; Han, C.M.; Qu, J.F.; Zhang, J.E.; Ao, S.J.; Guo, Q.Q.; Cleven, N.R.; Lin, S.F.; et al. Paleozoic multiple accretionary and collisional processes of the Beishan orogenic collage. *Am. J. Sci.* **2010**, *310*, 1553–1594. [CrossRef]
38. Gehrels, G.E.; Yin, A.; Wang, X.F. Detrital-zircon geochronology of the northeastern Tibetan Plateau. *Geol. Soc. Am. Bull.* **2003**, *115*, 881–896. [CrossRef]
39. Gehrels, G.E.; Yin, A.; Wang, X.F. Magmatic history of the northeastern Tibetan Plateau. *J. Geophys. Res. Solid Earth* **2003**, *108*, 2423. [CrossRef]
40. Xiao, W.J.; Windley, B.F.; Yong, Y.; Yan, Z.; Yuan, C.; Liu, C.Z.; Li, J.L. Early Paleozoic to Devonian multiple-accretionary model for the Qilian Shan, NW China. *J. Asian Earth Sci.* **2009**, *35*, 323–333. [CrossRef]
41. Song, S.G.; Niu, Y.L.; Su, L.; Xia, X.H. Tectonics of the North Qilian orogen, NW China. *Gondwana Res.* **2013**, *23*, 1378–1401. [CrossRef]
42. Song, D.F.; Xiao, W.J.; Collins, A.S.; Glorie, S.; Han, C.M.; Li, Y.C. New chronological constraints on the tectonic affinity of the Alxa block, NW China. *Precambrian Res.* **2017**, *299*, 230–243. [CrossRef]
43. Chen, X.H.; Yin, A.; Gehrels, G.E.; Cowgill, E.S.; Grove, M.; Harrison, T.M.; Wang, X.F.; Yang, N.; Liu, J. Mesozoic N-S extension in the eastern Altyn Tagh range on the northern margin of the Qinghai-Tibet Plateau. *J. Geomech.* **2004**, *10*, 193–212, (Chinese with English abstract).
44. Shao, H.H.; Chen, X.H.; Zhang, D. The Early Cretaceous tectonic deformation stages and detrital zircon U–Pb ages of Pingshanhu Basin in Hexi Corridor. *Geol. China* **2019**, *46*, 1079–1093. (In Chinese with English abstract). [CrossRef]
45. Dai, S.; Fang, X.M.; Song, C.H.; Gao, J.P.; Gao, D.L.; Li, J.J. Early tectonic uplift of the northern Tibetan Plateau. *Chin. Sci. Bull.* **2005**, *50*, 1642–1652. [CrossRef]
46. Peng, N. Basin Analysis and Paleogeography in North Qilian Mountain to Beishan Area, Early Cretaceous. Ph.D. Thesis, China University of Geosciences (Beijing), Beijing, China, 2013.

47. Wang, W.T.; Zhang, P.Z.; Pang, J.Z.; Garzione, C.N.; Zhang, H.P.; Liu, C.C.; Zheng, D.W.; Zheng, W.J.; Yu, J.X. The Cenozoic growth of the Qilian Shan in the northeastern Tibetan Plateau: A sedimentary archive from the Jiuxi Basin. *J. Geophys. Res. Solid Earth* **2016**, *121*, 2235–2257. [CrossRef]
48. Wang, W.T.; Zhang, P.Z.; Yu, J.X.; Wang, Y.Z.; Zheng, D.W.; Zheng, W.J.; Zhang, H.P.; Pang, J.Z. Constraints on mountain building in the northeastern Tibet: Detrital zircon records from synorogenic deposits in the Yumen Basin. *Sci. Rep.* **2016**, *6*, 27604. [CrossRef]
49. Cheng, F.; Jolivet, M.; Guo, Z.; Lu, H.; Zhang, B.; Li, X.; Zhang, D.; Zhang, C.; Zhang, H.; Wang, L.; et al. Jurassic–Early Cenozoic tectonic inversion in the Qilian Shan and Qaidam Basin, North Tibet: New insight from seismic reflection, isopach mapping, and drill core data. *J. Geophys. Res. Solid Earth* **2019**, *124*, 12077–12098. [CrossRef]
50. Yang, J.S.; Meng, F.C.; Zhang, J.X.; Li, H.B. The shoshonitic volcanic rocks at Hongliuxia: Pulses of the Altyn Tagh fault in Cretaceous? *Sci. China Ser. D Earth Sci.* **2001**, *44*, 94–102. [CrossRef]
51. Chen, S.; Wang, H.; Wei, J.; Lv, Z.Y.; Gan, H.J.; Jin, S.D. Sedimentation of the Lower Cretaceous Xiagou Formation and its response to regional tectonics in the Qingxi Sag, Jiuquan Basin, NW China. *Cretac. Res.* **2014**, *47*, 72–86. [CrossRef]
52. Jolivet, M.; Brunel, M.; Seward, D.; Xu, Z.Q.; Yang, J.S.; Roger, F.; Tapponnier, P.; Malavieille, J.; Arnaud, N.; Wu, C.L. Mesozoic and Cenozoic tectonics of the northern edge of the Tibetan Plateau: Fission-track constraints. *Tectonophysics* **2001**, *343*, 111–134. [CrossRef]
53. Pan, B.; Li, Q.; Hu, X.; Geng, H.; Liu, Z.; Jiang, S.; Yuan, W. Cretaceous and Cenozoic cooling history of the eastern Qilian Shan, northeastern margin of the Tibetan Plateau: Evidence from apatite fission-track analysis. *Terra Nova* **2013**, *25*, 431–438. [CrossRef]
54. Tian, Z.; Xiao, W.J.; Zhang, Z.; Lin, X. Fission-track constraints on superposed folding in the Beishan orogenic belt, southernmost Altaids. *Geosci. Front.* **2016**, *7*, 181–196. [CrossRef]
55. Gillespie, J.; Glorie, S.; Xiao, W.; Zhang, Z.; Collins, A.S.; Evans, N.; McInnes, B.; Grave, J.D. Mesozoic reactivation of the Beishan, southern Central Asian Orogenic Belt: Insights from low-temperature thermochronology. *Gondwana Res.* **2017**, *43*, 107–122. [CrossRef]
56. He, P.J.; Song, C.H.; Wang, Y.D.; Meng, Q.Q.; Chen, L.H.; Yao, L.J.; Huang, S.H.; Feng, W.; Chen, S. Cenozoic deformation history of the Qilian Shan (northeastern Tibetan Plateau) constrained by detrital apatite fission-track thermochronology in the northeastern Qaidam Basin. *Tectonophysics* **2018**, *749*, 1–11. [CrossRef]
57. Mao, Q.G.; Xiao, W.J.; Fang, T.H.; Wang, J.B.; Sun, M.; Yuan, C. Late Ordovician to early Devonian adakites and Nb-enriched basalts in Liuyuan area, Beishan, NW China: Implications for early Paleozoic slab-melting and crustal growth in the southern Altaids. *Gondwana Res.* **2012**, *22*, 534–553. [CrossRef]
58. Niu, Y.; Liu, C.; Shi, G.R.; Lu, J.; Xu, W.; Shi, J. Unconformity-bounded Upper Paleozoic megasequences in the Beishan Region (NW China) and implications for timing of Paleo-Asian Ocean closure. *J. Asian Earth Sci.* **2018**, *167*, 11–32. [CrossRef]
59. Li, J.; Wu, C.; Li, X.; Zuza, A.V.; Haproff, P.J.; Yin, A.; Shao, Z. Tectonic evolution of the Beishan orogen in central Asia: Subduction, accretion, and continent-continent collision during the closure of the Paleo-Asian Ocean. *Geol. Soc. Am. Bull.* **2023**, *135*, 819–851. [CrossRef]
60. Li, S.; Wang, T.; Wilde, S.A.; Tong, Y.; Hong, D.; Guo, Q. Geochronology, petrogenesis and tectonic implications of Triassic granitoids from Beishan, NW China. *Lithos* **2012**, *134–135*, 123–145. [CrossRef]
61. Zuo, G.; Zheng, Y. A new discovery of early Yanshanian strike-slip compressional nappe zones on middle–southern segment of Beishan Mts, Gansu. *Chin. J. Geol.* **1992**, *4*, 309–316. (In Chinese with English abstract).
62. Zheng, Y.D.; Zhang, Q.; Wang, Y.; Liu, R.G.; Wang, S.G.; Zuo, G.C.; Wang, S.Z.; Lkaasuren, B.; Badarch, G.; Badamgarav, Z. Great Jurassic thrust sheets in Beishan (North Mountains)-Gobi areas of China and southern Mongolia. *J. Struct. Geol.* **1996**, *18*, 1111–1126. [CrossRef]
63. Zhang, J.; Cunningham, D. Kilometer-scale refolded folds caused by strike-slip reversal and intraplate shortening in the Beishan region, China. *Tectonics* **2012**, *31*, TC3009. [CrossRef]
64. Liu, K.; Chen, X.; Zuza, A.V.; Shao, Z.; Qin, X.; Han, L.; Zhang, Y.; Yu, W.; Wang, Z.; Shi, X.; et al. The Late Mesozoic Intracontinental Contraction–Extension Transition in the Beishan Fold-Thrust Belt, Central Asia: Constraints From Structural Analysis and Apatite (U–Th)/He Thermochronology. *Tectonics* **2023**, *42*, e2022TC007532. [CrossRef]
65. Johnson, C.L.; Constenius, K.C.; Graham, S.A.; Mackey, G.; Menotti, T.; Payton, A.; Tully, J. Sedimentary and structural records of late Mesozoic high-strain extension and strain partitioning, East Gobi basin, southern Mongolia. *Geol. Soc. Am. Mem.* **2001**, *194*, 413–433. [CrossRef]
66. Meng, Q.R.; Hu, J.M.; Jin, J.Q.; Zhang, Y.; Xu, D.F. Tectonics of the late Mesozoic wide extensional basin system in the China–Mongolia border region. *Basin Res.* **2003**, *15*, 397–415. [CrossRef]
67. Peng, N.; Liu, Y.Q.; Kuang, H.W.; Chen, J.; Xue, P.L.; Xu, J.L.; Liu, H.; Liu, Y.X.; Xu, H.; Dong, C. The provenance of Lower Cretaceous basin in the Qilian Mountain-Beishan area: Evidence from paleocurrents, gravels, sandstone compositions and detrital zircon geochronology. *Geol. Bull. China* **2013**, *32*, 456–475, (Chinese with English abstract).

68. Yang, L.; Zhu, L.D.; Zheng, R.C.; Yang, W.G.; Wang, C.S. Sedimentary characteristics and tectonic setting of the Lower Cretaceous strata in Jiuxi Basin, Gansu. *Northwest. Geol.* **2011**, *44*, 112–118, (Chinese with English abstract).
69. Gao, R.; Li, T.D.; Wu, G.J. Lithospheric evolution and geodynamic process of the Qinghai–Tibet Plateau: An inspiration from the Yadong–Golmud–Ejin geoscience transect. *Geol. Rev.* **1998**, *44*, 389–395. (In Chinese with English abstract).
70. No. 4 Institute of Geology and Mineral Exploration, Gansu Provincial Bureau of Geology and Mineral Exploration and Development. *1:250,000 Formation Structural Map of the Huahai Sheet, Gansu Province [Map]*; Scale 1:250,000; No. 4 Institute of Geology and Mineral Exploration: Jiuquan, China, 2011.
71. Sanità, E.; Lardeaux, J.-M.; Marroni, M.; Gosso, G.; Pandolfi, L. Deciphering large-scale superposed fold systems at shallow crustal levels in collision zones: Insights from the Marguareis Massif (southwestern Alps). *J. Maps* **2021**, *17*, 571–580. [CrossRef]
72. Peng, N.; Kuang, H.W.; Liu, Y.Q. Sedimentary evolution and palaeogeography of the Early Cretaceous basins from the northern Qilian Mountains to Jiuxi areas. *Earth Sci. Front.* **2011**, *18*, 77–87, (Chinese with English abstract).
73. Yang, S.F.; Chen, H.L.; Cheng, X.G.; Xiao, A.C.; He, G.Y.; Chen, J.J.; Tian, D.W. Deformation characteristics and rules of spatial change for the Northern Qilian Shan thrust belt. *Earth Sci. Front.* **2007**, *14*, 211–221, (Chinese with English abstract).
74. No. 3 Institute of Geology and Mineral Exploration, Gansu Provincial Bureau of Geology and Mineral Resources. *Formation Structural Map of the Jiayuguan City Sheet, Gansu Province (Public Version) [Map]; Scale 1:250,000*; No. 3 Institute of Geology and Mineral Exploration, Gansu Provincial Bureau of Geology and Mineral Resources: Lanzhou, China, 2011. (In Chinese)
75. Davis, G.H. Tectonic klippe served the needs of cult worship, Sanctuary of Zeus, Mount Lykaion, Peloponnese, Greece. *GSA Today* **2017**, *27*, 4–9. [CrossRef]
76. Riba, O. Syntectonic unconformities of the Alto Cardener, Spanish Pyrenees: A genetic interpretation. *Sediment. Geol.* **1976**, *15*, 213–233. [CrossRef]
77. Suppe, J.; Chou, G.T.; Hook, S.C. Rates of folding and faulting determined from growth strata. In *Thrust Tectonics*; McClay, K.R., Ed.; Chapman & Hall: London, UK, 1992; pp. 105–121. [CrossRef]
78. Storti, F.; Poblet, J. Growth stratal architectures associated to décollement folds and fault-propagation folds: Inferences on fold kinematics. *Tectonophysics* **1997**, *282*, 353–373. [CrossRef]
79. Vergés, J.; Marzo, M.; Muñoz, J.A. Growth strata in foreland settings. *Sediment. Geol.* **2002**, *146*, 1–9. [CrossRef]
80. Zhang, C.C.; Wang, H.; Chen, S.; Yu, J.J.; Liao, Y.T.; Lu, Z.S.; Wei, J. Lacustrine basin fills in an Early Cretaceous half-graben, Jiuquan Basin, NW China: Controlling factors and implications for source rock depositional processes and heterogeneity. *J. Earth Sci.* **2019**, *30*, 158–175. [CrossRef]
81. Li, B.; Chen, X.; Shi, Z.; Ma, Y.; Li, X.; Zuza, A.V.; Wang, Z.; Wang, Y.; Xu, S.; Wang, Z. Cenozoic Kinematic Evolution of the Northern Tibetan Plateau: Implication for the Tectonic Setting of Deep Brines Mineralization in the Southwestern Qaidam Basin. *Tectonics* **2025**, *44*, e2024TC008525. [CrossRef]
82. Zuza, A.V.; Cheng, X.G.; Yin, A. Testing models of Tibetan Plateau formation with Cenozoic shortening estimates across the Qilian Shan–Nan Shan thrust belt. *Geosphere* **2016**, *12*, 501–532. [CrossRef]
83. Paton, C.; Woodhead, J.D.; Hellstrom, J.C.; Hergt, J.M.; Greig, A.; Maas, R. Improved laser ablation U–Pb zircon geochronology through robust downhole fractionation correction. *Geochem. Geophys. Geosyst.* **2010**, *11*, Q0AA06. [CrossRef]
84. Huang, C.; Wang, H.; Yang, J.H.; Ramezani, J.; Yang, C.; Zhang, S.B.; Yang, Y.H.; Xia, X.P.; Feng, L.J.; Lin, J.; et al. SA01—A proposed zircon reference material for microbeam U-Pb age and Hf-O isotopic determination. *Geostand. Geoanal. Res.* **2020**, *44*, 103–123. [CrossRef]
85. Gehrels, G.E.; Kapp, P.; DeCelles, P.G.; Pullen, A.; Blakey, R.; Weislogel, A.; Ding, L.; Guynn, J.; Martin, A.; McQuarrie, N.; et al. Detrital zircon geochronology of pre-Tertiary strata in the Tibetan-Himalayan orogen. *Tectonics* **2011**, *30*, TC5016. [CrossRef]
86. Sharman, G.R.; Sharman, J.P.; Sylvester, Z. detritalPy: A Python-based toolset for visualizing and analysing detrital geothermochronologic data. *Depos. Rec.* **2018**, *4*, 202–215. [CrossRef]
87. Saylor, J.E.; Sundell, K.E. Quantifying comparison of large detrital geochronology data sets. *Geosphere* **2016**, *12*, 203–220. [CrossRef]
88. Vermeesch, P. Multi-sample comparison of detrital age distributions. *Chem. Geol.* **2013**, *341*, 140–146. [CrossRef]
89. Saylor, J.E.; Jordan, J.C.; Sundell, K.E.; Wang, X.M.; Wang, S.Q.; Deng, T. Topographic growth of the Jishi Shan and its impact on basin and hydrology evolution, NE Tibetan Plateau. *Basin Res.* **2018**, *30*, 544–563. [CrossRef]
90. Meng, Y.; Tang, S.; Li, X.; Li, Y.; Bu, T. LA-ICP-MS zircon U-Pb dating of the Early Silurian clastic rocks in Dacaotan of Jiayuguan, North Qilian orogenic belt. *Geol. Bull. China* **2018**, *37*, 734–746. (In Chinese with English abstract).
91. Yang, J.H.; Du, Y.S.; Cawood, P.A.; Xu, Y.J. Silurian collisional suturing onto the southern margin of the North China Craton: Detrital zircon geochronology constraints from the Qilian Orogen. *Sediment. Geol.* **2009**, *220*, 95–104. [CrossRef]
92. Pfiffner, O.A. Thick-skinned and thin-skinned tectonics: A global perspective. *Geosciences* **2017**, *7*, 71. [CrossRef]
93. Butler, R.W.H.; Bond, C.E.; Cooper, M.A.; Watkins, H. Interpreting structural geometry in fold-thrust belts: Why style matters. *J. Struct. Geol.* **2018**, *114*, 251–273. [CrossRef]
94. Nabavi, S.T.; Fossen, H. Thrust and nappe tectonics in orogenic settings—A historical review. *Earth-Sci. Rev.* **2025**, *266*, 105139. [CrossRef]

95. Dennis, J.G.; Price, R.A.; Sales, J.K.; Hatcher, R.; Bally, A.W.; Perry, W.J.; Laubscher, H.P.; Williams, R.E.; Elliott, D.; Norris, D.K.; et al. What is a thrust? What is a nappe? *Geol. Soc. Lond. Spec. Publ.* **1981**, *9*, 7–9. [CrossRef]
96. Bollinger, L.; Avouac, J.P.; Beyssac, O.; Catlos, E.J.; Harrison, T.M.; Grove, M.; Goffé, B.; Sapkota, S. Thermal structure and exhumation history of the Lesser Himalaya in central Nepal. *Tectonics* **2004**, *23*, TC5015. [CrossRef]
97. Wissing, S.B.; Pfiffner, O.A. Structure of the eastern Klippen nappe (BE, FR): Implications for its Alpine tectonic evolution. *Eclogae Geol. Helv.* **2002**, *95*, 381–398. [CrossRef]
98. Wissing, S.B.; Pfiffner, O.A. Numerical models for the control of inherited basin geometries on structures and emplacement of the Klippen nappe (Swiss Prealps). *J. Struct. Geol.* **2003**, *25*, 1213–1227. [CrossRef]
99. Cleveland, C.; Garrard, R.M.; McLemore, D.M.; Yon, J.C.E.; Kidman, G.C.; MacLean, J.S. Strain accommodation in the footwall of the Rubys Inn thrust fault, Hillsdale Canyon, southern Utah. *Compass Earth Sci. J. Sigma Gamma Epsil.* **2014**, *86*, 102–117. [CrossRef]
100. Huang, X.; Gao, R.; Li, W.; Xiong, X. Seismic reflection evidence of crustal duplexing and lithospheric underthrusting beneath the western Qilian Mountains, northeastern margin of the Tibetan Plateau. *Sci. China Earth Sci.* **2021**, *64*, 96–109. [CrossRef]
101. Song, D.F.; Xiao, W.J.; Windley, B.F.; Han, C.M. Provenance and tectonic setting of late Paleozoic sedimentary rocks from the Alxa tectonic belt (NW China): Implications for accretionary tectonics of the southern Central Asian orogenic belt. *Geol. Soc. Am. Bull.* **2021**, *133*, 253–276. [CrossRef]
102. Wu, C.; Yin, A.; Zuza, A.V.; Zhang, J.Y.; Liu, W.C.; Ding, L. Pre-Cenozoic geologic history of the central and northern Tibetan Plateau and the role of Wilson cycles in constructing the Tethyan orogenic system. *Lithosphere* **2016**, *8*, 254–292. [CrossRef]
103. Xu, Y.J.; Du, Y.S.; Cawood, P.A.; Guo, H.; Hu, H.; An, Z.H. Detrital zircon record of continental collision: Assembly of the Qilian Orogen, China. *Sediment. Geol.* **2010**, *230*, 35–45. [CrossRef]
104. Bovet, P.M.; Ritts, B.D.; Gehrels, G.; Abbink, A.O.; Darby, B.; Hourigan, J. Evidence of Miocene crustal shortening in the North Qilian Shan from Cenozoic stratigraphy of the western Hexi Corridor, Gansu Province, China. *Am. J. Sci.* **2009**, *309*, 290–329. [CrossRef]
105. Lease, R.O.; Burbank, D.W.; Zhang, H.; Liu, J.; Yuan, D. Cenozoic shortening budget for the northeastern edge of the Tibetan Plateau: Is lower crustal flow necessary? *Tectonics* **2012**, *31*, TC3011. [CrossRef]
106. Wang, W.T.; Zhang, P.Z.; Zheng, W.J.; Zheng, D.W.; Liu, C.C.; Xu, H.Y.; Zhang, H.P.; Yu, J.X.; Pang, J.Z. Uplift-driven sediment redness decrease at ~16.5 Ma in the Yumen Basin along the northeastern Tibetan Plateau. *Sci. Rep.* **2016**, *6*, 29568. [CrossRef]
107. He, P.; Song, C.; Wang, Y.; Chen, L.; Chang, P.; Wang, Q.; Ren, B. Cenozoic exhumation in the Qilian Shan, northeastern Tibetan Plateau: Evidence from detrital fission track thermochronology in the Jiuquan Basin. *J. Geophys. Res. Solid Earth* **2017**, *122*, 6910–6927. [CrossRef]
108. Zheng, D.; Clark, M.K.; Zhang, P.; Zheng, W.; Farley, K.A. Erosion, fault initiation and topographic growth of the North Qilian Shan (northern Tibetan Plateau). *Geosphere* **2010**, *6*, 937–941. [CrossRef]
109. Zhuang, G.S.; Johnstone, S.A.; Hourigan, J.; Ritts, B.D.; Robinson, A.; Sobel, E.R. Understanding the geologic evolution of northern Tibetan Plateau with multiple thermochronometers. *Gondwana Res.* **2018**, *58*, 195–210. [CrossRef]
110. Kapp, P.; Murphy, M.A.; Yin, A.; Harrison, T.M.; Ding, L.; Guo, J.H. Mesozoic and Cenozoic tectonic evolution of the Shiquanhe area of western Tibet. *Tectonics* **2003**, *22*, 1029. [CrossRef]
111. Zhao, Z.B.; Bons, P.D.; Stübner, K.; Wang, G.H.; Ehlers, T.A. Early Cretaceous exhumation of the Qiangtang Terrane during collision with the Lhasa Terrane, central Tibet. *Terra Nova* **2017**, *29*, 382–391. [CrossRef]
112. Ma, Y.M.; Yang, T.S.; Bian, W.W.; Jin, J.J.; Wang, Q.; Zhang, S.H.; Wu, H.C.; Li, H.Y.; Cao, L.W. A stable southern margin of Asia during the Cretaceous: Paleomagnetic constraints on the Lhasa–Qiangtang collision and the maximum width of the Neo-Tethys. *Tectonics* **2018**, *37*, 3853–3876. [CrossRef]
113. Lai, W.; Hu, X.M.; Garzanti, E.; Xu, Y.W.; Ma, A.L.; Li, W. Early Cretaceous sedimentary evolution of the northern Lhasa terrane and the timing of initial Lhasa–Qiangtang collision. *Gondwana Res.* **2019**, *73*, 136–152. [CrossRef]
114. Kapp, P.; DeCelles, P.G. Mesozoic–Cenozoic geological evolution of the Himalayan–Tibetan orogen and working tectonic hypotheses. *Am. J. Sci.* **2019**, *319*, 159–254. [CrossRef]
115. Cogné, J.-P.; Kravchinsky, V.A.; Halim, N.; Hankard, F. Late Jurassic–Early Cretaceous closure of the Mongol–Okhotsk Ocean demonstrated by new Mesozoic palaeomagnetic results from the Trans-Baïkal area, SE Siberia. *Geophys. J. Int.* **2005**, *163*, 813–832. [CrossRef]
116. Van der Voo, R.; van Hinsbergen, D.J.J.; Domeier, M.; Spakman, W.; Torsvik, T.H. Latest Jurassic–earliest Cretaceous closure of the Mongol–Okhotsk Ocean: A paleomagnetic and seismological–tomographic analysis. In *Late Jurassic Margin of Laurasia–A Record of Faulting Accommodating Plate Rotation*; Geological Society of America Special Paper 513; Anderson, T.H., Didenko, A.N., Johnson, C.L., Khanchuk, A.I., MacDonald, J.H., Jr., Eds.; Geological Society of America: Boulder, CO, USA, 2015; pp. 589–606. [CrossRef]
117. Ren, Q.; Zhang, S.H.; Wu, Y.B.; Yang, T.S.; Gao, Y.B.; Turbold, S.; Zhao, H.Q.; Wu, H.C.; Li, H.Y.; Fu, H.; et al. New Late Jurassic to Early Cretaceous paleomagnetic results from North China and southern Mongolia and their implications for the evolution of the Mongol–Okhotsk suture. *J. Geophys. Res. Solid Earth* **2018**, *123*, 10370–10398. [CrossRef]

118. Ma, Q.; Xu, Y.G. Magmatic perspective on subduction of the Paleo-Pacific plate and initiation of the big mantle wedge in East Asia. *Earth-Sci. Rev.* **2021**, *213*, 103473. [CrossRef]
119. Wang, X.F.; Zhang, Z.C.; Guo, Z.J.; Zhang, C. Geochemical characteristics and tectonic significance of the Early Cretaceous volcanic rocks in the southern margin of Jiuxi Basin. *Geol. J. China Univ.* **2004**, *10*, 569–577. (In Chinese with English abstract).
120. Li, H.B.; Yang, J.S. Evidence for Cretaceous uplift of the northern Qinghai–Tibetan Plateau. *Earth Sci. Front.* **2004**, *11*, 345–359.
121. Dewey, J.F. Extensional collapse of orogens. *Tectonics* **1988**, *7*, 1123–1139. [CrossRef]
122. Wu, C.; Zuza, A.V.; Li, J.; Haproff, P.J.; Yin, A.; Chen, X.H.; Ding, L.; Li, B. Late Mesozoic–Cenozoic cooling history of the Qilian Shan and northern Tibetan Plateau. *Geol. Soc. Am. Bull.* **2021**, *133*, 2393–2417. [CrossRef]

Disclaimer/Publisher's Note: The statements, opinions and data contained in all publications are solely those of the individual author(s) and contributor(s) and not of MDPI and/or the editor(s). MDPI and/or the editor(s) disclaim responsibility for any injury to people or property resulting from any ideas, methods, instructions or products referred to in the content.